July 10, 2018

Announcements

- Wednesday, July 11, 2:30 pm, CSNE (Optional): Pomodoro Writing Session.

- Thursday, July 12, 9:00-10:30 am, CSNE (Required): “The CSNE and Industry” – a seminar by Dr. Scott Ransom, Director of CSNE Industry Relations and Innovation

- Friday, July 13, noon, Harborview Medical Center (Optional, RSVP needed): UW Neurosurgery Seminar by Zachary Stephen, Ph.D. titled “Clinical Application of Nanoparticles”

Poster Presentations

- Opportunity to focus your efforts.
- Initial public exhibition of your research.
- Promote you hard work.
- Make contacts for the future.

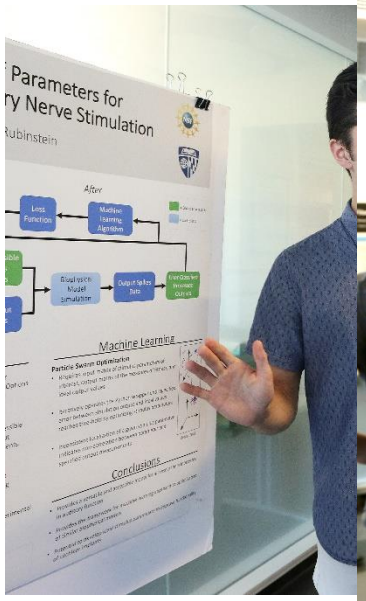

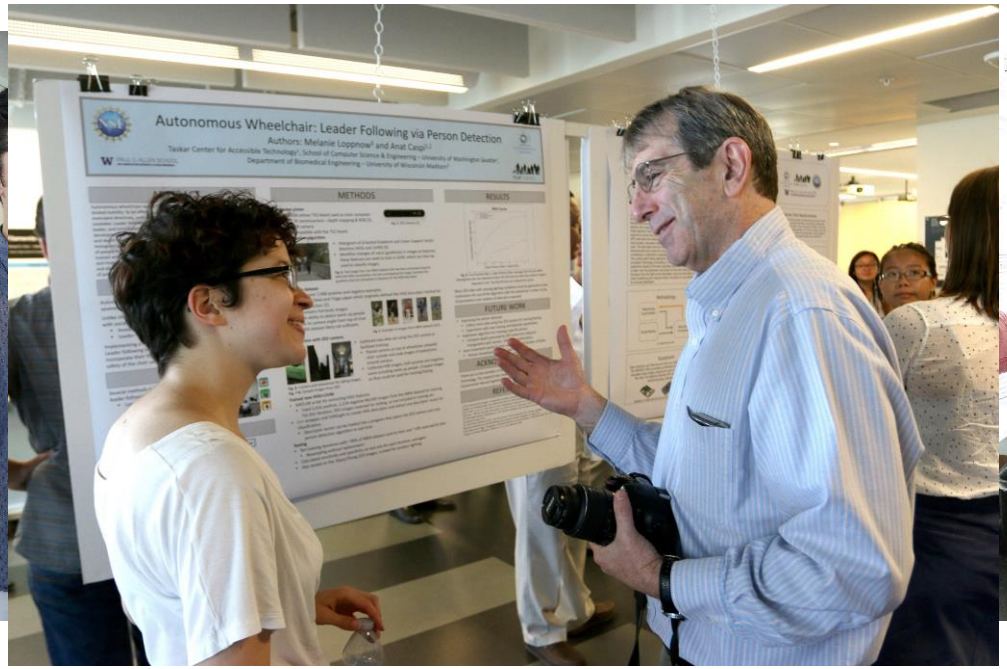

Posters vs. Talks

	Poster	Talk
Difficulty to Prepare		
Time to Prepare		
Audience Reached		
Stress Level		

Poster Mechanics

Dimensions for *CSNE Research Symposium*

Foam Board = 48” x 36”

Your Poster = 44” x 32” (allows a margin)

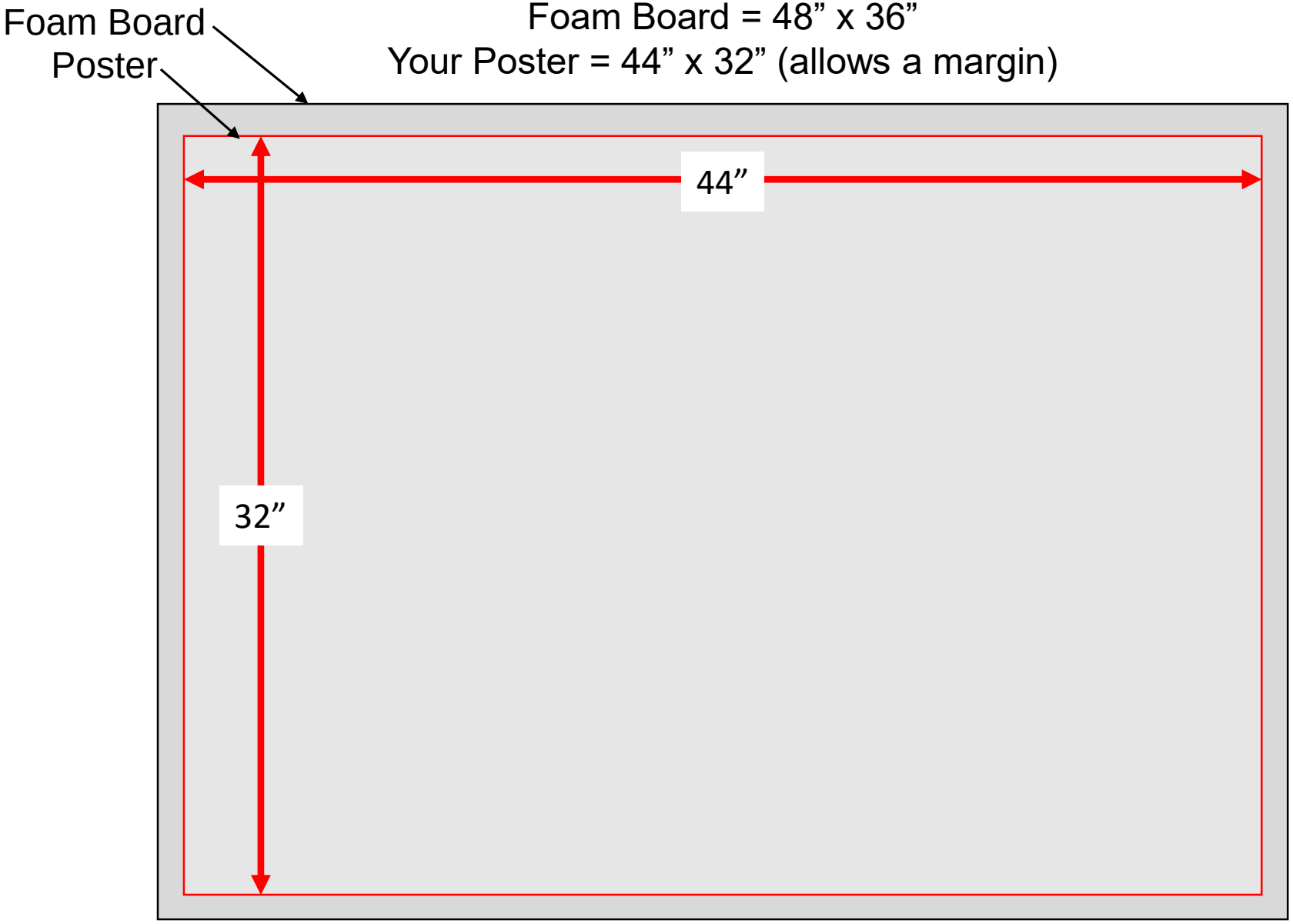

Poster Mechanics

Background

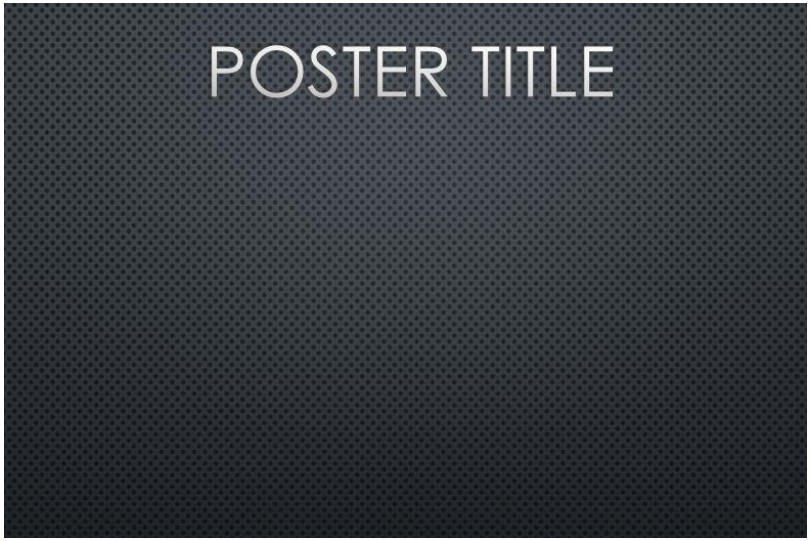

Titles

- First (only?) thing that people
- Encourage (lure) people to your poster
- Include a question: yes or no?
- Define scope of the study
- Include a significant result or finding
- Not too long
- Like a newspaper headline

Title Review

- Share potential title with people seated near you.
- Revise title?
- Share title(s) with group.

Poster Mechanics

Required Components

1. **Title**
2. **Authors (you will be the first author; lab director likely last; mentors and others in the middle)**
3. **Affiliations (Departments, Universities, City, State)**
4. **CSNE Logo (download from class web site)**
5. **NSF Logo (download from class web site)**
6. **Grant Acknowledgment Statement (download from class web site)**

Poster Mechanics

Suggested Components

1. UW Logo
2. Your Home University Logo
3. Section headings

    A. Introduction
    B. Methods
    C. Results
    D. Discussion
    E. References (optional)

Poster Mechanics

Hints and Tips

1. Know your audience.
2. Less is usually better than more.
3. Simplify graphics (if possible), but use them.
4. Text should be readable from a distance.
5. Use PowerPoint, Illustrator, InDesign…
6. Do not justify paragraph margins.
7. Avoid poor resolution graphics.
8. Be careful with color.
9. Be careful with busy backgrounds.
10. Submit in PDF (chudler@uw.edu)

Poster Critique

- Teams of two students
- Each team has two posters
- Spend ~5 min/poster
  - Layout/organization/style
  - Content
  - Font
  - Color
    - Background?
- Present to group (1-2 min/poster)

Dorsal root ganglia neural recordings with a novel non-penetrating thin-film microelectrode array

Zachariah J. Sperry[1,2], John P. Seymour[3], Fan Wu[3], Shani E. Ross[1,2], Kanghwan Kim[3], John T. Bentley[1,2], Euisik Yoon[3], Tim M. Bruns[1,2]

1. Biomedical Engineering, University of Michigan, Ann Arbor
2. Biointerfaces Institute, University of Michigan, Ann Arbor
3. Electrical Engineering and Computer Sciences, University of Michigan, Ann Arbor

BIOMEDICAL ENGINEERING
UNIVERSITY OF MICHIGAN

Peripheral Neural Engineering and Urodynamics Lab

DRG as Neural Interface

Dorsal root ganglia (DRG) are clusters of **sensory cell bodies** just outside of the spinal cord.

Recording and decoding neural information from the DRG gives insight regarding peripheral sensory systems for investigating neurophysiology and developing neural prostheses.

Current **microelectrode** interfaces can record from **single neurons**, but the shanks must be introduced by **penetrating the epineurium**.

These arrays were designed for the cortex and are not well matched to DRG morphology.

Additonally they can **cause inflammatory response and scarring**.

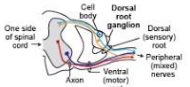

Anatomy of the spinal cord and nerve roots (horizontal section)

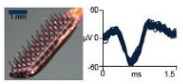

Blackrock penetrating electrode array and recorded single-neuron waveforms

Device **design should be driven by anatomical data**, both qualitative and quantitative. For example, penetrating electrode shank lengths for motor cortex are often chosen to record from layer 5 neurons.

GOAL: *To design, fabricate, and evaluate a novel microelectrode array for neural recording in the DRG.*

DRG Anatomy » Device Design

DRG anatomical observations:

- On the scale of microelectrode arrays, DRG are curved rather than flat, so array should **curve or conform to the surface**.
- DRG cells bodies are concentrated near the dorsal surface, so advantageous to **record primarily in this upper layer** (see below for quantitative analysis).
- The epithelial layer is thin enough (25-100 μm) to record through, potentially allowing a **non-penetrating dorsal surface** approach.

Previous studies with recording single units from the surface of neural tissue:

- Cortex (Khodagholy et al. 2014)
- DRG (Gaunt & Bruns 2011). The DRG electrodes used required downward force to make good contact, but ideally an array would **require only surface tension**.

DRG cross-section showing edges (red = DRG, blue = cell body, green = nucleus)

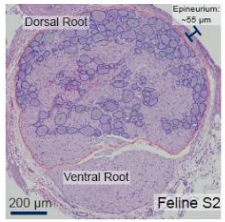

Cell bodies (blue pixels) transformed to a circular area for comparative analysis [inset: transform method]

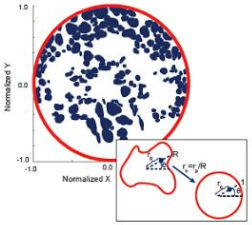

Average ratio of cellular pixels to normalized area by annular sector.

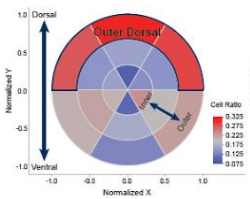

Pixel ratios by annular sector. Regions that are not connected by same letter are significantly different

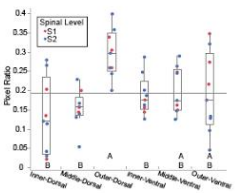

Novel Thin-Film Array

Array specifications:

- 64 channels
- Polyimide substrate [3.6 μm thick]
- Gold interconnects [400 nm thick]
- Iridium electrode sites
  - 1130 μm² & 400 μm²
  - Impedance: 173 & 369 (±35) kΩ
  - 4 sets of "pentrodes" (5 closely spaced sites)

Thin-film array schematic. Pentrode sites are circled.

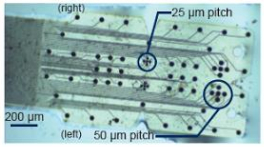

Surgery and *In Vivo* Recordings

After laminectomy to expose the spinal roots, array was placed on the **L7 DRG** of a feline under isoflurane anesthesia. **Surface tension was used** to secure the array.

In vivo image of thin-film array on L7 DRG

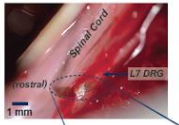

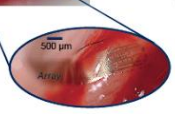

Recorded neural activity (30 kHz) with Ripple Grapevine system. Sorting offline.

Single- and multi-unit activity observed during cutaneous dermatome brushing and joint flexion on **35/64 unique channels.**

Maps of electrode site activity by activity type, 2 different stimuli, 2 different array placements. Black oval indicates the approximate region of observed activity.

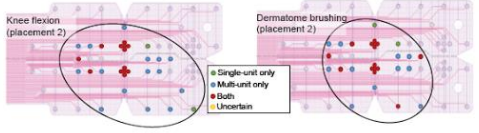

Single- and multi-unit waveforms for dermatome brushing trial. Gray boxes indicate (approximate) stim periods

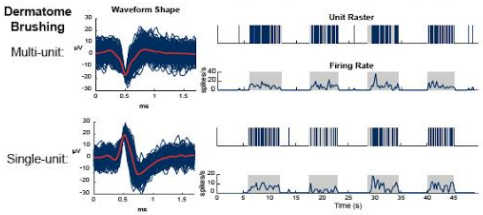

Raw voltage recording from dermatome brushing trial containing large single-unit activity. SNR calculation illustrated for large unit.

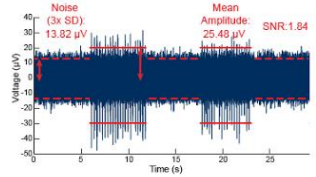

SNR for all identified waveforms, by activity type

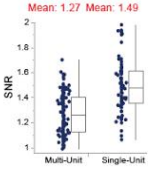

Source Localization

In some trials, **simultaneous single-unit activity** was observed on all five sites in a **pentrode** (3/4 pentrode sites; both 25 μm & right 50 μm).

Assuming a **point-current** source in a **homogeneous medium**:

$$V = \frac{k}{\sqrt{x^2 + y^2 + z^2}} \qquad k = \frac{I}{4\pi\sigma} \text{ ,assumed constant}$$

V: Voltage | **x, y, z**: Cartsian distances from source | **I**: Current | **σ**: Conductivity

Linear algebraic techniques for tetrode (Lee et al. 2007) estimate signal source location as the **intersection of 5 source-electrode radius estimates** from each site.

For a pentrode, four estimates of location can be made.

Estimate **required site curvature estimate**. Curve radius chosen was 500 μm.

Location estimates were only possible for 25 μm pentrode sites. Estimate for the 50 μm pentrode did not converge to a reasonable solution.

Simultaneous action potentials on pentrode channels (joint flexion)

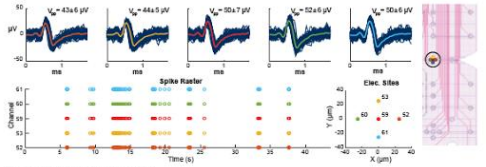

Neuron source location estimate (side view over typical DRG histology section)

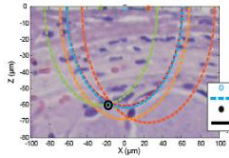

(top view)

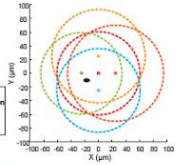

Conclusions & Future Work

Using a conforming thin-film array, we successfully recorded from the DRG surface. We observed both single- and multi-unit activity. Waveforms on pentrode sites contained spatial information used to estimate signal source, which is a novel analysis in DRG.

Going forward, we will refine the **array layout** by increasing the number of polytrode sites and shaping it for the DRG profile as supported by by the NIH SPARC program. We will use source localization to **explore DRG neurophysiology** and anatomy by mapping activity with different stimuli.

Finally, we will explore **electrical stimulation** and **chronic array placement** toward therapeutic goals (ex. bladder neuroprosthesis).

Acknowledgements

I would like to acknowledge pNEURO Lab members Kaile Bennett, Abeer Khurram, Anastasia Ostrowski, and Chris Stephan.

The array was manufactured at the Lurie Nanofabrication Facility at the University of Michigan.

Funding provided by the Craig H. Neilsen Foundation (Grant #314980) and by the University of Michigan MiBrain Initiative.

LNF UNIVERSITY OF MICHIGAN
BIO INTERFACES INSTITUTE
NEUROSCIENCE INSTITUTE
CRAIG-H NEILSEN FOUNDATION
pneurolab.com

Whole genome computational analysis of tRNA-derived small RNAs in Arabidopsis thaliana RNA biogenesis mutants

Wojciech Karlowski, Agnieszka Thompson, Patrycja Plewka, Maciej Szymanski, Andrzej Zielezinski, Przemyslaw Nuc, Artur Jarmolowski

Department of Computational Biology & Department of Gene Expression, Adam Mickiewicz University in Poznan, Poland

http://combio.pl

ABSTRACT

In recent years, application of the high-throughput sequencing technologies revealed a novel class of abundant, **stable, non-coding RNAs, derived from tRNA (tRFs).** Using Arabidopsis thaliana as a model organism, we aim at identification and characterization of the components involved in tRNA and microRNA biogenesis pathways that may play a role in generation of tRFs.

We are presenting our results of a global characterization of small RNAs originating from Arabidopsis tRNA and tRNA-like genomic sequences. In addition to our own experimental data from over **20 A. thaliana strains** carrying mutations in genes associated with tRNA and microRNA biogenesis, the set includes all high quality Arabidopsis short RNA sequences from public sRNA-Seq databases. Thus, the entire dataset provides a broad perspective of tRNA-derived short RNAs in Arabidopsis for a wide cross-section of tissues, developmental stages, as well as biotic and abiotic stress conditions. An advanced and user-friendly exploration of datasets and results of the analyses were implemented in a form of the "**T-regs**" web portal.

INTRODUCTION

tRF types:

tRFs: short RNA fragments derived from tRNA

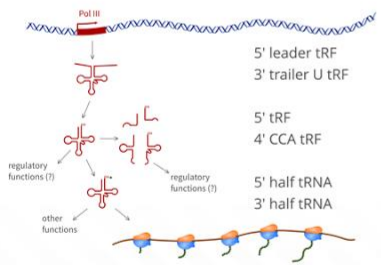

METHOD

Data processing schema (Arabidopsis as model organism)

MATERIALS

RNA biogenesis mutants

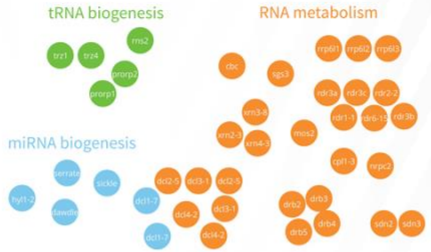

Public samples: environmental / stress

tRNA genes: GtRNAdb / TAIR 10

638 genes / 237 unique sequence variants / 48 anticodons

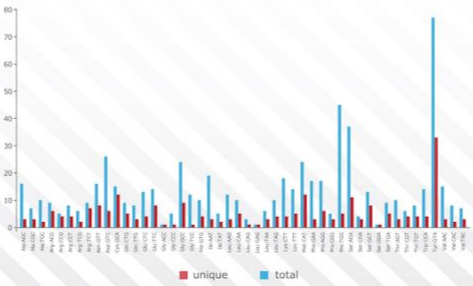

RESULTS

tRNA-Seq: re-annotation of tRNA

tRNA expression in shoot and root tissues

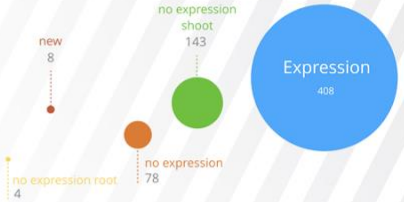

tRNA-Seq: landscape of tRNA expression

log[tRNA-Arg/tRNA-Met(i)]

t-Regs: tRFs database

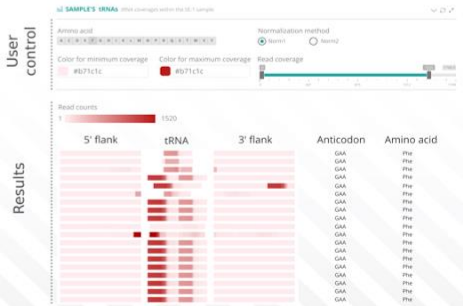

ACKNOWLEDGMENTS

This work was supported by grant from the National Science Center 2011/03/B/NZ2/01416 and the KNOW RNA Research Centre 809 in Poznan (No. 01/KNOW2/2014)

RISK SCIENCE CENTER

GEEK OUT ON THE SCIENCE OF RISK

Providing accessible educational resources on risk science using YouTube

NEED

EVIDENCE-INFORMED DECISIONS on human health require at least a rudimentary understanding of the science underlying potential risks

MEMBERS OF THE PUBLIC and others want more accessible, understandable and credible information on health risks

OVER 1 BILLION UNIQUE USERS visit YouTube each month worldwide, watching over 6 billion hours of video per month

SCIENCE EDUCATION CHANNELS like SciShow and Minute Physics have upward of 2 million subscribers

RISK BITES WAS CREATED in response to an opportunity to use YouTube in a unique and powerful way to help people understand the basic principles of evidence-informed approaches to understanding and addressing risk

CHALLENGE

LACK OF TALENT: Videos were constrained to the limited drawing and video making abilities of the main contributors

LACK OF TIME: Videos needed to be produced on top of a busy academic workload

TO BE SUCCESSFUL, the channel needed to post regular, high quality videos that appealed to a broad audience, while providing useful information

LACK OF RESOURCES: Limited equipment was available

PROCESS

Story Board

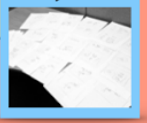

Script

Narration & Backing

Video

Closed Captions

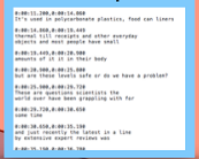

Final Video

IMPACT

An integrated strategy of dissemination using social media and networks is used to raise awareness

VIEWING TIME: Viewers currently spend approximately 450 hours per month watching RiskBites videos - the equivalent of 19 days per month

VIEWS: Risk Bites videos currently receives around 13,000 views per month

QUALITATIVE INDICATORS OF SUCCESS: More qualitative indicators of success include word of mouth from users, link sharing, and the degree to which professional organizations actively use and share the videos

CLOSED CAPTIONS: All videos have English subtitles for the hearing-impared

Andrew Maynard PhD, Director, University of Michigan Risk Science Center

IRENA FENG, GUETCHYN MILLIEN AND MARIA RAMIREZ, PULMONARY CENTER, BOSTON UNIVERSITY SCHOOL OF MEDICINE

Analysis of a mutant mouse model lacking histone3-lysine27 N-methyltransferase EZH2 in developing lung epithelium

ABSTRACT

Histone modification is important for epigenetic regulation of gene expression. Histone3-lysine27 N-methyltransferase EZH2 is part of a protein group called the polycomb repressive complex-2 (PRC2) and primarily plays a role in gene silencing by adding three methyl groups to H3K27, causing chromatin to condense and silencing the genes encoded in the condensed DNA. The role of EZH2 as to which genes are silenced and which are expressed in the developing lung is not clear. Using homologous recombination, mice were genetically engineered such that the promoter for signaling pathway gene *Sonic hedgehog* (*Shh*) drives the expression of Cre recombinase. Since developing lung epithelium cells express *Shh*, the expression of Cre recombinase combined with the insertion of *LoxP* sites in the introns of *Ezh2* led to the removal of EZH2 from developing lung epithelium in this knock-out model. We report successful confirmation of the absence of the EZH2 protein in the lung epithelium at different embryonic developmental stages by genotyping with PCR and analyzing phenotypes by fluorescent immunohistochemistry. Mice homozygous for the removed Ezh2 alleles had phenotypically abnormal lung development during late gestation. Consequently, this mouse model may allow for further study of the role of EZH2 in lung development and its effects on gene expression.

INTRODUCTION

DNA is packaged around histones in the cell nucleus, and the way the DNA is packaged is important for gene expression. Histone expression is dynamic and can be changed by methylation of lysine residue of the histones. Methylation of H3K27 has been shown to be affiliated with gene silencing. EZH2 is important for maintaining cell fate and differentiation by silencing genes during development and is the main methyltransferase for H3K27. Mutations in EZH2 result in developmental problems such as Weaver syndrome.

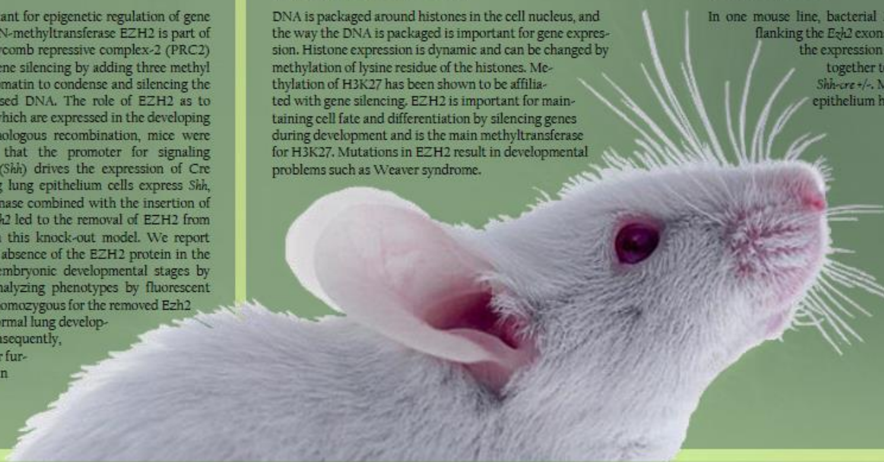

METHODS

In one mouse line, bacterial *LoxP* sites were inserted into the introns of *Ezh2* flanking the *Ezh2* exons. For another mouse line, the promoter of *Shh* drives the expression of Cre recombinase. These two lines were then bred together to create the mutant mice, which is both *Ezh2 fl/fl* and *Shh-cre +/-*. Mutant mice die at birth. Lungs that lack Ezh2 in the epithelium have smaller alveolar sacs and a thicker mesenchyme.

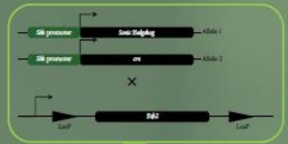

MUTANT MOUSE MODEL

- Cre recombinase is expressed where *Shh* is expressed during development
- Thus, Cre recombinase removes the *Ezh2* gene in lung epithelia
- Genotyping using PCR to detect alleles
- Absence of Ezh2 was confirmed through fluorescent immunohistochemistry using an antibody against Ezh2

RESULTS

FLUORESCENT IMMUNOHISTOCHEMISTRY

Different developmental time points were evaluated using an antibody against Ezh2. Slides were also stained with DAPI to visualize the nuclei, and the two images were overlaid to see where staining for Ezh2 showed.

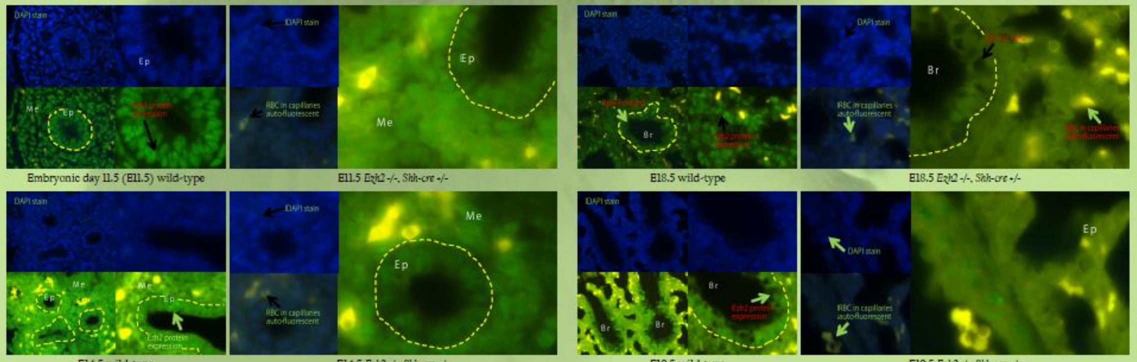

Embryonic day 11.5 (E11.5) wild-type; E11.5 *Ezh2* -/-, *Shh-cre* +/-; E18.5 wild-type; E18.5 *Ezh2* -/-, *Shh-cre* +/-

E14.5 wild-type; E14.5 *Ezh2* -/-, *Shh-cre* +/-; E19.5 wild-type; E19.5 *Ezh2* -/-, *Shh-cre* +/-

Br = bronchiole, Ep = epithelium, Me = mesenchyme, RBC = red blood cell

PCR

To genotype the mice, PCR was used to detect individual alleles. Samples were run on a 2% agarose gel during gel electrophoresis.

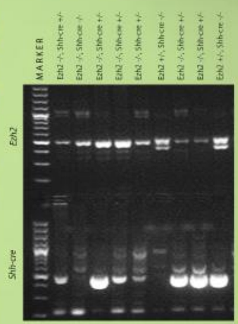

CONCLUSION

In mutant mice, the majority of the Ezh2 protein was knocked out in the lung epithelium. The presence of Ezh2 in some of the lung epithelia indicates that Cre recombination was not complete. The incomplete knockout of Ezh2 depends on the half-life of Cre recombinase and its expression; if Cre activity is not strong enough, Ezh2 may not be knocked out in that cell, leading to signal during immunohistochemistry.

Next step: to stain for the expression of activated Cre recombinase and to compare its expression pattern to that of Ezh2 in the mutant mice.

REFERENCES

Conerly, M.L., MacQuarrie, K.L., Fong, A.P., Yao, Z., and Tapscott, S.J. (2011). Polycomb-mediated repression during terminal differentiation: what don't you want to be when you grow up? Genes and Development 25, 997-1003.

Herriges, M. and Morrisey, E.E. (2014). Lung development: orchestrating the generation and regeneration of a complex organ. Development 141, 502-513.

Longmire, T.A., Ikonomou, L., Hawkins, F., Christodoulou, C., Cao, Y., Jean, J.C., Kwok, L.W., Mou, H., Rajagopal, J., Shen, S.S., Dowton, A.A., Serra, M., Weiss, D.J., Green, M.D., Snoeck, H.W., Ramirez, M.I., and Kotton, D.N. (2012). Efficient Derivation of Purified Lung and Thyroid Progenitors from Embryonic Stem Cells. *Cell Stem Cell* 10, 398-411.

Millien, G., Beane, J., Lenburg, M., Tsao, P.N., Lu, J., Spira, A., and Ramirez, M. I. (2008). Characterization of the mid-foregut transcriptome identifies genes regulated during lung bud induction. *Gene Expression Patterns* 8, 124-139.

Morrisey, E.E., Cardoso, W.V., Lane, R.H., Rabinovitch, M., Abman, S.H., Ai, X., Albertine, K.H., Bland, R.D., Chapman, H.A., Checkley, W., Epstein, J.A., Kintner, C.R., Kumar, M., Minoo, P., Mariani, T.J., McDonald, D.M., Mukouyama, Y.S., Prince, L.S., Reese, J., Rossant, J., Shi, W., Sun, X., Werb, Z., Whitsett, J.A., Gail, D., Blaisdell, C.J., and Lin, Q.S. (2013). Molecular Determinants of Lung Development. *Annals of the American Thoracic Society* 10, S12-S16.

O'Carroll, D., Erhardt, S., Pagani, M., Barton, S.C., Surani, M.A., and Jenuwein, T. (2001). The Polycomb-Group Gene Ezh2 Is Required for Early Mouse Development. *Molecular and Cellular Biology* 21, 4330-4336.

Sparmann, A., and van Lohuizen, M. (2006). Polycomb silencers control cell fate, development and cancer. *Nature Review Cancer* 6, 846-856.

DATA FLOW ANALYSIS IN THE PRESENCE OF CORRELATED CALLS

Marianna Rapoport, Ondřej Lhoták, Frank Tip
University of Waterloo

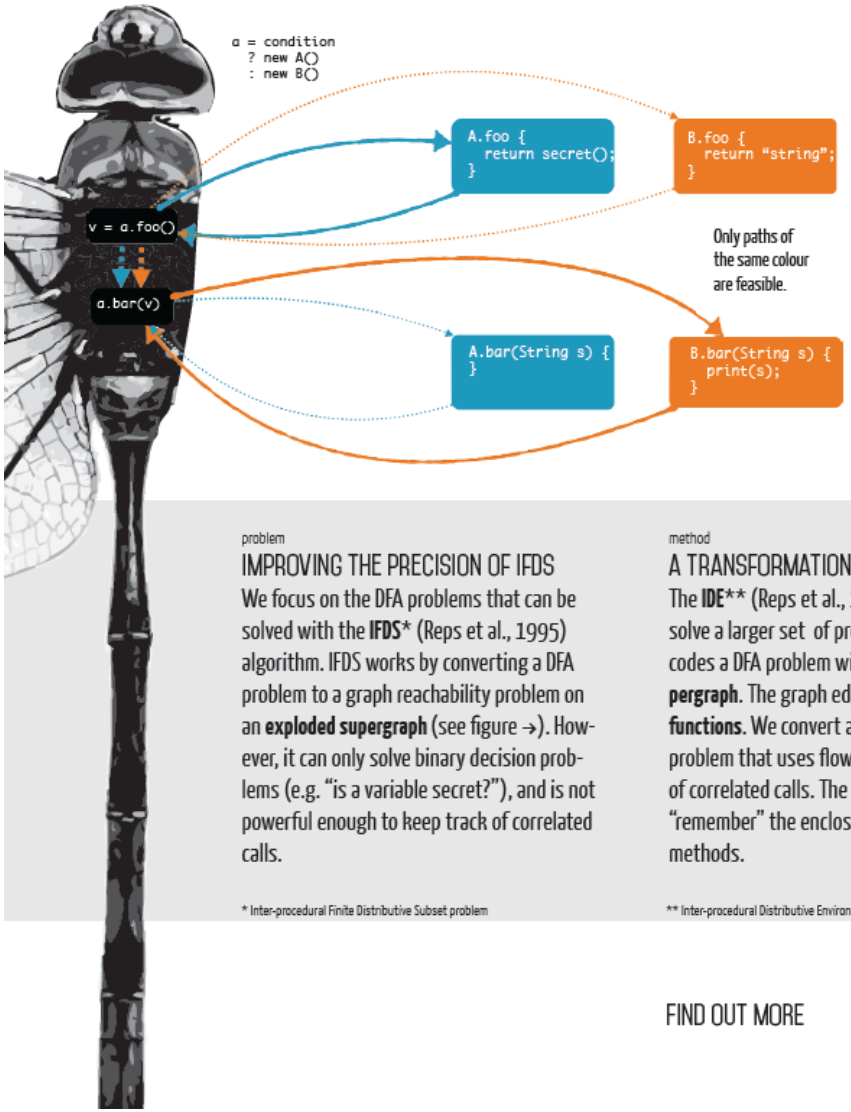

summary

THE PRECISION OF DATA-FLOW ANALYSES CAN BE IMPROVED IN THE PRESENCE OF CORRELATED CALLS.

intro

IS YOUR DATA REALLY SECRET?

Data-flow analysis (DFA) approximates properties of programs without running them. For instance, in a **taint analysis**, we find out which variables are **secret**, e.g. to discover confidential information leaks. However, **infeasible paths** in a program's control-flow graph can affect the accuracy of an analysis.

goal

ELIMINATE INFEASIBLE PATHS

An infeasible path is one that cannot occur during program execution. In an object-oriented language, two method calls are **correlated** if they dispatch to multiple targets. The goal of this work is to **eliminate** the infeasible paths caused by correlated calls.

result

CORRELATED CALLS ANALYSIS

The correlated calls analysis improves the precision of IFDS results that contain correlated calls. Infeasible paths caused by correlated calls are removed by transforming an IFDS problem into a special type of IDE problem and solving the latter.

problem

IMPROVING THE PRECISION OF IFDS

We focus on the DFA problems that can be solved with the **IFDS*** (Reps et al., 1995) algorithm. IFDS works by converting a DFA problem to a graph reachability problem on an **exploded supergraph** (see figure →). However, it can only solve binary decision problems (e.g. "is a variable secret?"), and is not powerful enough to keep track of correlated calls.

* Inter-procedural Finite Distributive Subset problem

method

A TRANSFORMATION FROM IFDS TO IDE

The **IDE**** (Reps et al., 1996) algorithm can solve a larger set of problems than IFDS. IDE encodes a DFA problem with a **labeled exploded supergraph**. The graph edges are labeled with **flow functions**. We convert an IFDS problem to an IDE problem that uses flow functions to keep track of correlated calls. The flow functions serve to "remember" the enclosing classes of dispatched methods.

** Inter-procedural Distributive Environment problem

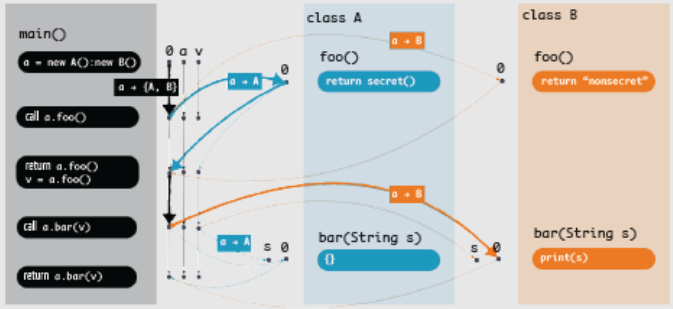

FIND OUT MORE

- How do IFDS and IDE work?
- How are flow functions represented?
- How can we implement the correlated-calls analysis?
- How do we know the analysis is correct?

cs.uwaterloo.ca/~mrapopor

UNIVERSITY OF Southampton

Inside a Feather

Laminar Layup Varies Around and Along Bird Feather Shafts

Since feathered flight developed more than 150 million years ago, the central shaft of a bird feather has evolved under selection pressures to become light, stiff, and strong. As a result, the shaft has become a complex, fibre-reinforced biocomposite beam.

In quantifying the mechanical properties of feather shafts, previous researchers have reported values of flexural rigidity which vary over two orders of magnitude. Some of this variation can be explained by changes in geometry. However, the laminar layup of the shaft cortex and the micromechanics of these laminae have not yet been considered.

We have previously shown that the number of laminae varies between species of birds, and that these laminae are anisotropic (Laurent *et al.* 2014). This variation means that it is necessary to understand not only the geometry of feather shafts, but also their laminar layup and the micromechanics of those laminae before we can understand and predict the macromechanical behaviour of the feather shaft.

Here, we present data gathered at different locations on a feather shaft (rachis and calamus) using Synchrotron Radiation Computed Tomography (SR-CT). This gives us a detailed insight into the laminar layup and the orientation of the internal fibres. This is the first step in understanding the mechanical properties of feather shafts from the inside.

Method

The Swiss Light Source (SLS), at the Paul Scherrer Institute (Switzerland), is a third-generation synchrotron light source. It provides a high-brightness photon beam which enables CT scanning at resolutions three orders of magnitude higher than a typical hospital-based scanner, with scan times as short as six minutes. With these scans, we capture the three-dimensional void orientation in rachis material. Using transmission electron microscopy, these voids were found to be aligned with the internal fibres.

Samples (L = 5 mm) were removed from the leading flight feather of a Whooper Swan (*Cygnus cygnus*) at 10, 30, 50, 70, and 90% of the shaft length and scanned. Overlapping regions of interest were stitched together and the whole sample was reconstructed with voxel dimensions of 325 nm. The largest sample (10%) required 42 individual scans and the smallest (90%) only six. Scans were stitched together using a Fourier-shift algorithm where possible, or with the 'MosaicJ' tool in ImageJ/Fiji.

Results & Conclusion

Our SR-CT scans reveal geometry of the shaft changing along the length of the feather. Looking more closely they show how the number, orientation, and thickness of laminae vary within the shaft. Therefore, our results show that laminar layup varies around, and along, a bird feather shaft.

These variations in geometry and laminae influences the rachis mechanics. Next, to fully understand the implication for the feather mechanics, we will determine the modulus of individual laminae.

Flight feathers are light, strong and stiff and allow heavy birds, such as a whooper swan, *Cygnus cygnus*, to fly.

Each flight feather has a shaft, which changes in geometry along its length, like the second flight feather (pictured).

Ultra high resolution Computed Tomography reveals that the number and thickness of differently oriented laminae varies around and along the feather shaft.

LAURENT, CM[1,2] | SCHNEIDER, P[1] | DYKE, GJ[3] | BOARDMAN, RP[1] | PALMER, C[3,4] | COOK, RB[5] | DE KAT , R[1]

[1]Aerodynamics and Flight Mechanics, Engineering and the Environment, University of Southampton, UK
[2]Ocean and Earth Science, National Oceanography Centre Southampton, UK
[3]Bioengineering, Engineering and the Environment, University of Southampton, UK
[4]Department of Evolutionary Zoology and Human Biology, University of Debrecen, Hungary
[5]X-Ray Centre for Computed Tomography, University of Southampton, UK
[6]Earth Sciences, University of Bristol, UK
[7]nCATS national Centre for Advanced Tribology, Engineering and the Environment, University of Southampton, UK

Reference:
Nanomechanical properties of bird feather rachises: exploring naturally occurring fibre reinforced laminar composites
Christian M. Laurent, Colin Palmer, Richard P. Boardman, Gareth Dyke, Richard B. Cook
J. R. Soc. Interface 2014 11 20140961; DOI: 10.1098/rsif.2014.0961. Published 22 October 2014

EPSRC Engineering and Physical Sciences Research Council
National Oceanography Centre NATURAL ENVIRONMENT RESEARCH COUNCIL
NERC SCIENCE OF THE ENVIRONMENT
The Leverhulme Trust
PAUL SCHERRER INSTITUT PSI
SPITFIRE

Cloning, expression and characterization of GH10 xylanases from landfill leachate bacteria *Paenibacillus* sp. MAEPY2

Patric Chua[1*], Gary A Dykes[2], Lee Sui Mae[1]

[1]School of Science, Monash University, Malaysia
[2]School of Public Health, Curtin University, Australia
*Corresponding author e-mail: tcchu4@student.monash.edu

Background

Landfill wastes are usually materials with plant biomass, e.g. food/organic wastes, papers and horticultural wastes.

Major components in plant biomass can be degraded rapidly (in a few days) by soil microbes in landfills.

Plant biomass-degrading microbes can exploited for applications in various industrial processes.

Bioprospecting

Landfill leachate was collected from a local landfill site.

Figure 1: Leachate treatment pond at Jeram Sanitary Landfill, Selangor, Malaysia.

Sampling

Microbial population in leachate was cultured on minimal media containing cellulose.

Culture

Figure 2: *Paenibacillus* sp. MAEPY1 and MAEPY2 under Congo Red stain showing cellulolytic ability.

Screening

Isolates that were capable of degrading cellulose was isolated and identified as *Paenibacillus* sp. MAEPY1 and MAEPY2.

Isolation

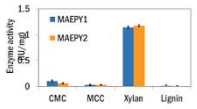

Figure 3: Enzyme activity (IU/mg) of *Paenibacillus* sp. MAEPY1 and MAEPY2 crude extracts against carboxymethyl cellulose (CMC), microcrystalline cellulose (MCC), xylan, and lignin.

Enzyme Assay

Enzyme activity of both isolates further tested against substrates of other plant cell wall components. Activity against xylan was the highest in comparison.

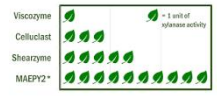

Figure 4: Comparison of xylanase activity of *Paenibacillus* sp. MAEPY2 against commercial products at 55°C, pH 6. *crude extract of *P.* sp. MAEPY2 was used as representative

Xylanase activity of crude enzyme extract was benchmarked against commercial enzymes. Results indicate great potential.

Read more:

Chua PTC, Yoo HS, Dykes G, Lee SM. 2015).Isolation and characterization of cellulose degrading ability in *Paenibacillus* isolates from landfill leachate. *Malaysian Journal of Microbiology* **11**: 185-194.

Sequencing

Whole genome of *Paenibacillus* sp. MAEPY2 was sequenced using the Illumina Miseq system. Draft genome sequence was registered in NCBI GenBank under the accession no. AWUK00000000.

Sequencing

39% of the open reading frames (ORFs) have not been assigned any functions.

21% of the ORFs are associated with carbohydrate metabolism.

Only 20 of the 585 ORFs are putative xylanases and xylosidases.

Gene annotation of *P.* sp. MAEPY2 genome was performed in the Rapid Annotations using Subsystems Technology (RAST) server[1]. Two putative GH10 xylanase genes were identified using the EXPASY tools[2] and BLAST (P).

Bioinformatics

- Glycosyl hydrolase family 10
- Length: 963 bp, 35.3 kDa
- Has signal peptide sequence
- Expressed as extracellular protein
- Predicted isoelectric point at 8.92

- Glycosyl hydrolase family 10
- Length: 1023 bp, 39.6 kDa
- No signal peptide sequence
- Expressed as a cytoplasmic protein
- Predicted isoelectric point at 5.10

Cloning and expression

Xyn4 and Xyn5 genes were cloned into pRSET-A with 6X His-tag and transformed into *E. coli* BL21 (DE3). Expression in host cells was induced using 1mM IPTG and overnight incubation at 30°C.

Cloning

Purification was performed for the His-tagged Xyn4 and Xyn5 using AKTA Purifier fast protein liquid chromatography (FPLC).

Expression

SDS-PAGE was performed following Laemmli's method[3]. A native-PAGE was performed for xylan zymography.

Purification

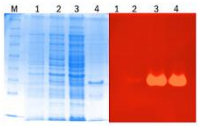

Figure 6: SDS-PAGE and zymogram analysis of the purified xylanases. Lane M: protein marker, 1-4: uninduced, induced, cell lysate, purified sample.

SDS-PAGE

Enzyme studies

Optimum temperature and pH were determined via xylanase activity assay. Thermal stability was determined by pre-incubating the enzyme at various temperatures without substrates, prior to assay.

Enzyme Assay

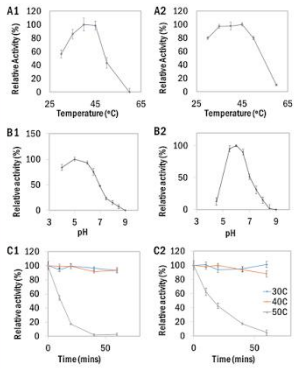

Figure 6: Effects of temperature and pH on enzyme activities of purified (1) Xyn4 and (2) Xyn5. (A) Enzyme activity was assayed at pH 7.4 and temperatures from 30°C to 60°C. (B) Enzyme activity was assayed at 40°C in 50 mM buffer systems. pH shown are represented by measured values after assay. (C) Temperature stability of the enzymes was determined at 30°C, 40°C, and 50°C, for 10, 20, 40 and 60 minutes.

In this study

We characterized two xylanase genes from *Paenibacillus* sp. MAEPY2.

Both xylanases are active from 30°C to 50°C, but work best at 40°C. Xyn4 is active at pH 4 to 7, while Xyn5 is active at pH 5 to 7.

NEXT STEPS:
A more detailed analysis of the enzyme-substrate specificity, i.e. hydrolysis products from xylooligosaccharides.

Please take one

Leave your comments here

Leave your contacts here

Please take one

Leave your comments here

Leave your contacts here

Acknowledgements

Funding for this study was provided by the Monash University Malaysia Tropical Medicine and Biology Multidisciplinary Platform. Commercial enzymes were graciously provided by Novozymes. We are grateful to Worldwide Landfills Sdn. Bhd. for their assistance in procuring the samples, and to Malaysian Genome Institute for providing technical advice.

References

1. Aziz et al. 2008. *BMC Genomics* 9: 75.
2. Gasteiger et al. 2003. *Nucleic Acids Res* 31: 3784-3788.
3. Laemmli, UK. 1970. *Nature* 227: 680-685.

MONASH University MALAYSIA

Integrative root biology: scaling across transporters, the rhizosphere, the root system, and the field

Larry M. York, Jonathan P. Lynch, John Foulkes, and Malcolm J. Bennett

Centre for Plant Integrative Biology
University of Nottingham, UK

Architectural and anatomical root phenes evolved greater nitrogen acquisition efficiency in maize

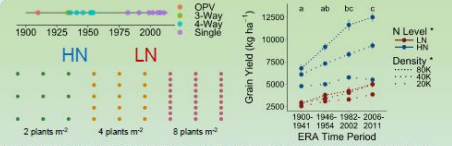

Sixteen hybrids from the past 100 years in the USA were grown at two nitrogen levels and three densities that represent historic and current agronomic conditions (above, left). Current material performed better in all conditions (above, right). Architectural and anatomical **root phenes evolved towards greater nitrogen acquisition efficiency** (see panel on right).

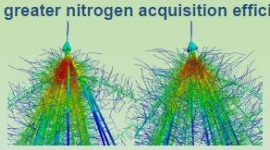

Modern material had fewer nodal roots, longer laterals, greater distance from the shoot to lateral emergence, and more shallow nodal root angles (left).

Aerenchyma, air filled spaces in the cortex, increased in low nitrogen soil and at greater population densities (right).

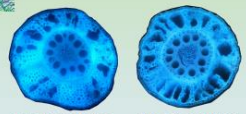

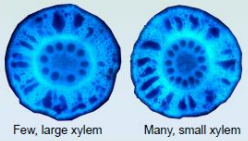

The number of xylem vessels, tubes for transporting water in the center of the root, increased while the area of each vessel decreased in modern material compared to old (left).

Intensive phenotyping of maize root crowns reveals phene integration that enhances nitrogen acquisition

Intensive phenotyping of maize root crowns involves removing whorls of roots and measuring root phenes including angle, number, and lateral root density and length on every whorl (above).

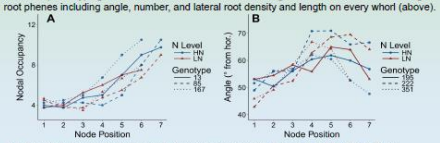

Phene states vary within maize root crowns, among genotypes, and exhibit plasticity to soil nitrogen levels, whether high or low, in the field (above).

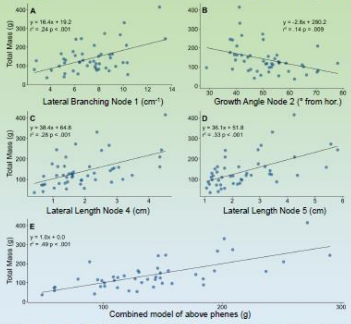

The relation of individual phenes to plant growth in the field are informative (A-D), but their integration (E) provides the most explanatory power using multiple regression (above).

Integrating the rhizosphere

Mucilage
P depletion
Microbes
N depletion

The rhizosphere was defined succinctly by Hiltner in 1904:

the soil influenced by roots

However, since that time research involving the rhizosphere has generally focused on subjects in which scientists have conceptualized, defined, and constrained the rhizosphere based on their research question.

Therefore, the rhizosphere has been inconsistently defined as the soil around roots in which microbial communities are altered, rhizodeposition occurs, pH is changed, or water / nutrients are depleted.

The rhizosphere is not any one of these zones, but is rather comprised of all these processes in which roots influence soil. Furthermore, these zones are not isolated but are overlapping and integrated processes that create a holistic rhizosphere.

Future research will focus on how rhizosphere processes influence one another, such as how mucilage affects soil porosity or nutrient uptake, and will require interdisciplinary methods.

Nitrate uptake kinetics

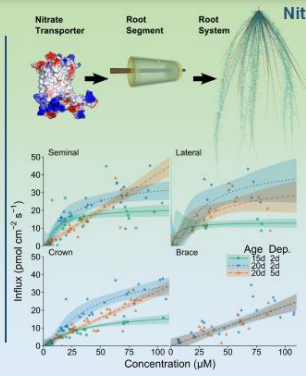

Most studies of nitrate uptake kinetics focused on whole root system uptake or only measured influx after down or up regulating nitrate transporters. How kinetics scale from the transporter to the whole root system is not well understood.

A PVC chamber was used to surround root segments from different root classes of a maize hybrid and loaded with nitrate solution of varying concentrations in order to determine influx. Michaelis-Menten parameters were determined:

$$I_n = \frac{I_{max}(C - C_{min})}{K_m + (C - C_{min})}$$

I_n net influx, I_{max} maximum influx rate, K_m concentration of half I_{max}

Nitrate uptake kinetics differed among root classes and were affected by the age of the plant and how long the plant was deprived of nitrate before being measured. In fact, in some contexts Michaelis-Menten kinetics were lost and linear kinetics were found instead, which may indicate passive uptake or a different transporter being expressed.

Published: York, L. M., Galindo-Castañeda, T., Schussler, J., and Lynch, J. P. (2016). Evolution of US maize (*Zea mays* L.) roots. *Journal of Experimental Botany* **66**, 2347-2358.
York, L. M., and Lynch, J. P. (2015). Intensive field phenotyping of maize (*Zea mays* L.) roots. *Journal of Experimental Botany* **66**, 5493-5505.

In Preparation: York, L. M., Carminati, A., Mooney, S. J., Ritz, K., and Bennett, M. J. Integrating rhizosphere zones, processes, and semantics. *Journal of Experimental Botany*, invited review for IGRR9
York, L. M., Silberbush, M., and Lynch, J. P. Nitrate uptake kinetics differ among root classes in maize and have additive effects with root system architecture. *Annals of Botany*.

Acknowledgements: Tania Galindo-Castañeda imaged the anatomical sections using laser ablation tomography. Simon Newstead kindly provided the NRT1.1 nitrate transporter electrostatic surface diagram.

www.rootbiologist.com

Topological signature in the NEXT high pressure xenon TPC

Paola Ferrario, Instituto de Física Corpuscular (Universitat de València-CSIC)
on behalf of the NEXT Collaboration

1 THE NEXT EXPERIMENT

NEXT is an experiment looking for neutrinoless double beta decay in a high pressure xenon TPC. It is located at the Canfranc Underground Laboratory (LSC), in the Spanish Pyrenees. It uses electroluminescence (EL) for energy measurement and tracking and has proven an excellent energy resolution (~0.74% FWHM extrapolated to the $Q_{\beta\beta}$ of Xe-136, i.e., 2.458 MeV) and topological signature for background rejection in prototypes. A first stage, NEW, with ~10 kg of xenon, is being commissioned at the LSC — see poster P4.066 for more details.

2 BACKGROUND IN NEXT

The main background in NEXT comes from high energy gammas from environmental radioactivity entering the active volume of the detector. When gammas interact with xenon gas, they can produce photoelectric and Compton electrons, at energies very similar to $Q_{\beta\beta}$. Electrons and muons coming from outside can be efficiently vetoed with fiducial cuts . See poster P4.065 for more details.

3 TRACK RECONSTRUCTION

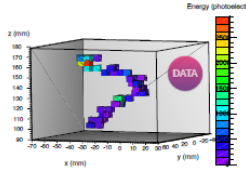

The current track reconstruction is based on the analysis of the charge detected in each time bin by an array of silicon photomultipliers placed behind the EL area. A search for 2D hits and a subsequent voxelization of the whole space is performed, and a Breadth First Search (BFS) algorithm is used to connect the voxels to form tracks. The algorithm sorts the voxels into tracks with a criterium of connectivity, which considers two voxels as connected if their centres are closer than a maximum distance. The algorithm also finds the end-points of a track as the voxels with maximum distance along the track.

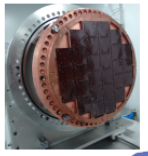

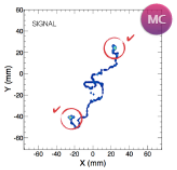

4 THE TOPOLOGICAL SIGNATURE

Electrons moving through xenon gas lose energy at an approximately fixed rate until they become non-relativistic. At the end of the trajectory they produce an energy 'blob', i.e., a high energy deposition in a small region. This feature can be used to distinguish background single-electrons (one 'blob' only) from signal double-electrons (two 'blobs').

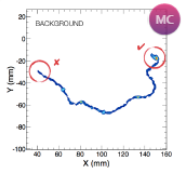

5 PROOF IN NEXT-DEMO

NEXT-DEMO was a 1-kg prototype, built and operated at IFIC, Valencia. We have demonstrated the power of topological cut using radioactive sources: Na-22 provides high energy electrons and Th-228 electron-positron pair production, to mimic background and signal respectively. A minimum threshold was imposed on the energy deposited at both ends of one track to pass the filter. A signal efficiency of 66.7% ± 0.9% and a background acceptance of 24.3% ± 1.3% is found, in good agreement with MC simulations.

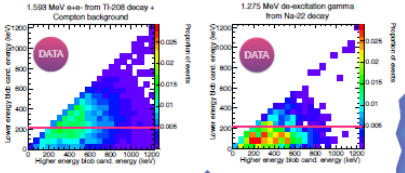

JHEP 1601 (2016) 104

6 EXPECTED PERFORMANCE IN NEW

NEW will be used for background and two-neutrino double beta decay measurements, as well as to prove energy resolution and the power of topological rejection at energies close to $Q_{\beta\beta}$. Simulations indicate a significant improvement of the topological rejection, due to the larger volume of the detector. First MC studies point to 66.9% ± 0.6% signal efficiency for 12.9% ± 0.6% background acceptance for the same analysis as in NEXT-DEMO at a pressure of 10 bar.

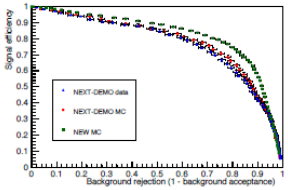

7 FUTURE IMPROVEMENTS

New reconstruction approaches are being investigated. The Maximum Likelihood Expectation Minimization method tries to solve the inverse problem of finding a set of energy depositions in the chamber, given the sensors response to the EL light. Given a statistical model that describes the forward problem, it provides estimates for the model's parameters, maximizing the likelihood of the model, given any outcome. We are also exploring the power of deep neural networks, which could be used for reconstruction and classification of events as signal or background, exploiting all possible features in the image.

NEUTRINO 2016 XXVII INTERNATIONAL CONFERENCE ON NEUTRINO PHYSICS AND ASTROPHYSICS 4 - 9 JULY 2016

This work was supported by the following agencies and institutions: the European Research Council (ERC) under the Advanced Grant 339787-NEXT; the Ministerio de Economía y Competitividad of Spain under grants CONSOLIDER-Ingenio 2010 CSD2008-0037 (CUP), FIS2014-53371-C04 and the Severo Ochoa Program SEV-2014-0398.

Ankyrin G membrane partners drive the establishment and maintenance of the axon initial segment

501.12 - G49

Christophe Leterrier[1], Nadine Clerc[1], Fanny Rueda Boroni[1], Audrey Montersino[1], Bénédicte Dargent[1], Francis Castets[1]

1- Aix Marseille University, CNRS, CRN2M UMR 7286, Marseille, France

The AIS, a nexus for neuronal physiology

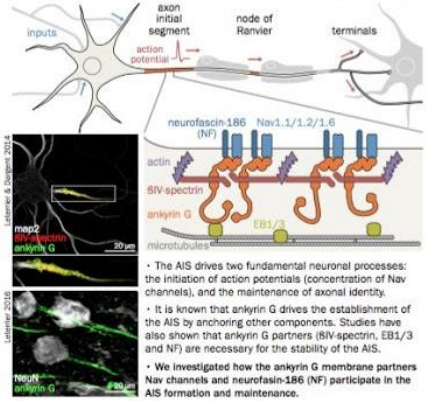

- The AIS drives two fundamental neuronal processes: the initiation of action potentials (concentration of Nav channels), and the maintenance of axonal identity.
- It is known that ankyrin G drives the establishment of the AIS by anchoring other components. Studies have also shown that ankyrin G partners (ßIV-spectrin, EB1/3 and NF) are necessary for the stability of the AIS.
- **We investigated how the ankyrin G membrane partners Nav channels and neurofasin-186 (NF) participate in the AIS formation and maintenance.**

Nav channels knockdown destabilizes the AIS

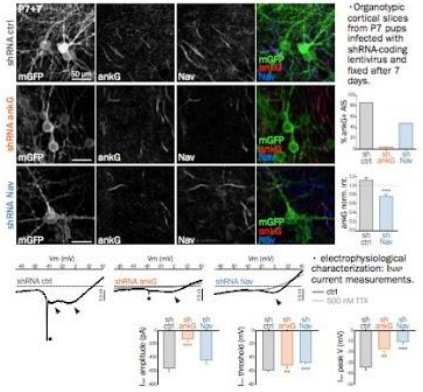

- Organotypic cortical slices from P7 pups infected with shRNA-coding lentivirus and fixed after 7 days.
- electrophysiological characterization: Nav current measurements.

Nav/NF knockdown impairs AIS maintenance

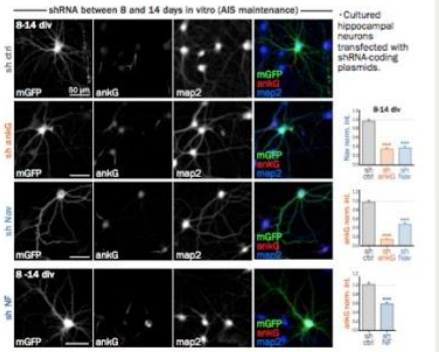

- Cultured hippocampal neurons transfected with shRNA-coding plasmids.

Nav/NF knockdown impairs AIS formation

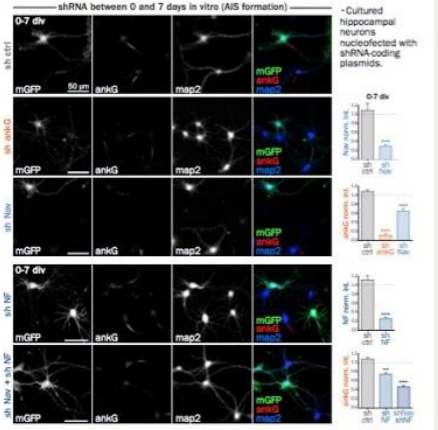

- Cultured hippocampal neurons nucleofected with shRNA-coding plasmids.

One membrane partner can rescue another

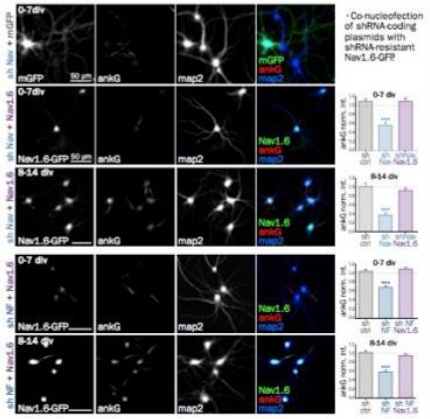

- Co-nucleofection of shRNA-coding plasmids with shRNA-resistant Nav1.6-GFP

Minimal ankG membrane partner: mABD

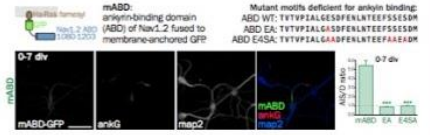

mABD expression rescues AIS formation

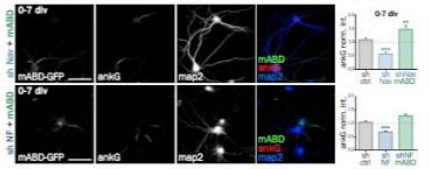

Modulation of AIS formation by mABD

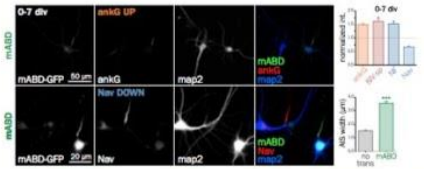

mABD mislocalize ankG in mature neurons

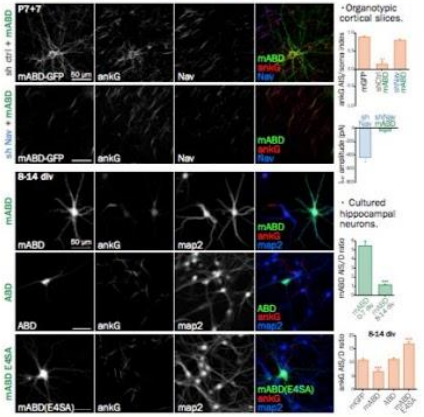

- Organotypic cortical slices.
- Cultured hippocampal neurons.

Conclusions & perspectives

- Membrane protein partners of ankyrin G (Nav channels pore-forming subunits, neurofascin-186) contribute to both AIS formation and maintenance in cultured neurons and organotypic slices.
- They stabilize the AIS by linking ankyrin G to to the plasma membrane, as shown by the rescue obtained with a synthetic membrane-anchored ankyrin-binding domain (mABD).
- Differential effects of mABD expression during and after AIS formation suggest a slot competition mechanism with endogenous Nav channels, and a co-transport of ankyrin G and its membrane partners to the AIS.

Judge a catalyst by its anions rather than by its ligands

"Judge a man by his questions rather than by his answers." — Voltair

Luca Biasiolo

mail: *luca.biasiolo@uniud.com*

supervisor: Daniele Zuccaccia

Questions? Look for this guy!

Introduction

Homogeneous gold catalysis represents a fast growing area in organic chemistry. [*Chem. Rev.* **2007**, *107*, 3180] In gold(I) catalyzed nucleophilic addition to a C–C unsaturated bond it is generally accepted that, if the rate determining step (RDS) is the nucleophilic attack, the more electron withdrawing ligands (that mean more activated substrate) will favor the reaction; whereas an inverse trend has been found when the RDS is the protodeauration. [*J. Am. Chem. Soc.* **2012**, *134*, 5697] On the other hand, also the anion plays an important role influencing the catalysis[1] but it is generally less considered. We decide to focus our effort on the rationalization of every single step of the mechanism studying this system through both experimental and theoretical approach.

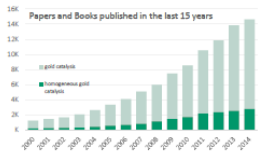

3 Protodeauration

During this step the most important factors are the affinity of X^- with H^+ and L-Au$^+$ (that depends also on the ligand properties).[4] The activity trends for the tested reaction show that **4** and **3** complexes follow the anion's basicity/coordination scale. While for PR_3 complexes the best anions are OTs^- and TFA^-, that interacting with Au waken the Au-C bond.[5]

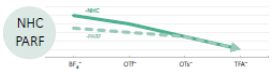

WANT MORE INFO?

Download the poster or visit us

https://aucat.thch.unipg.it/

AIM OF THE PROJECT

The scope of the project *"Overview of gold(I) catalyzed activation of unsaturated bonds: ligands and anions effects on the cycle."* is to fully study and understand all the steps that characterize gold(I) catalyzed reactions, focusing especially on the role of the Ion Pairs. Notwithstanding both nature of the ligand and counterion effects are considered among the most important factors in gold catalysis, a rational understanding of their synergy/antagonism is still lacking.

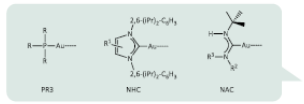

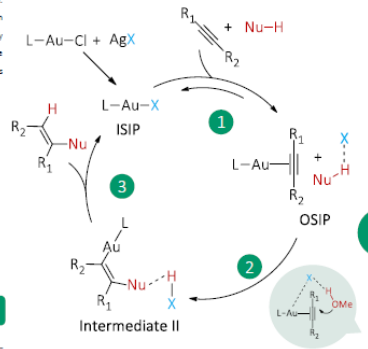

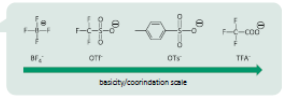

Experimental Details

Complexes: all the gold complexes were synthesized using the proper silver salt, used *in situ* or isolated, those stable were achieved in high yield and characterized by NMR spectroscopy.

Ion Pairs: through a systematic NMR (^{19}F-^1H HOESY) and DFT (Coulomb Potential) studies was possible to characterize all the IP.

Catalysis: we tested our catalysts in two model reactions both are easily followable by NMR spectroscopy. The activity was calculated as TOF = $[n_{product} \cdot n_{catalyst}^{-1}] \cdot min^{-1}$.

Works published during the PhD:

1. L. Biasiolo *et al.*, *Chem. Eur J.* **2014**, *20*, 14594.
2. G. Ciancaleoni *et al.*, *Organometallics* **2013**, *32*, 4444.
3. L. Biasiolo *et al.*, *Catal. Sci. Technol.* **2015**, 10.1039/C4CY01440E
4. G. Ciancaleoni, *et al.*, *Chem. Eur. J.* **2015**, *21*, 2467.
5. L. Biasiolo, *et al.*, *ACS Catal.* **2015**, Submitted.

1 OSIP structures

With OSIP we indicate the Outer Sphere Ion Pair that is formed during the catalytic cycle. In our firsts work we observed that the charge (⊕) is not placed over the gold, as generally represented, but it could be delocalized all over the complex depending on the latter structure.[2]

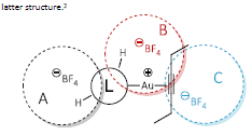

Ligands	A	B	C
1-2: PR_3		*	****
3: PArF		***	**
4: NHC(iPr)	***		**
5: NHC(BIAN)	**	*	**
6: NAC(H_2)	*****		
7: NAC(iPr-H_2)	***		**
8: NAC(pyr-H_2)	***		**
9: NAC(eph-H_2)	*	****	

1: R=Ph; 2: R=^{t}Bu; 3: BrArF; 4: R^1=H; 5: BIAN; 6: R^2=^{t}Bu, R^3=H; 7: R^2=R^3=iPr; 8: R^2-N-R^3=pyrrolidine; 9: R^2=Me, R^3=OMe-COHPh.

2 Nucleophilic Attack

Nature and position of the anion are crucial when the nucleophilic attack is the RDS. We chose the alkoxylation of alkynes, one of the oldest applications of gold(I) catalyst, as test reaction. Our experimental and theoretical experiment point out that the attack of the MeOH must be helped by the anion or by polarized additives.[3]

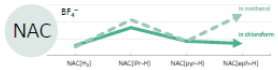

Using the NAC series we investigated how change the IP structure functionalizing the ligand and how turn it of with the solvents.[3]

With the NHC and PR_3 complexes we observed how the activity is strictly related to the basicity/coordination of the anion which is, in turn, related to the ligand coordination properties. [1, 4]

CONCLUSIONS

From our results, it is evident that the correct choice of L, in order to increase the performances of gold(I) complexes, strongly depends on the nature of the anion X$^-$ and *vice versa*.[5] The next step will be to apply this innovative thought pattern to other gold catalyzed reactions of industrial and biological interest. In fact the possibility to use gold, instead other metals (as Hg) or lewis acids, to activate C-C unsaturated bonds is a greener solution.

UNIVERSITÀ DEGLI STUDI DI UDINE

UNIVERSITÀ DEGLI STUDI DI PERUGIA

UNIVERSITÀ DEGLI STUDI DI NAPOLI

Consiglio Nazionale delle Ricerche

FIRB Fondo per gli Investimenti della Ricerca di Base

A Compartment Model for the Transport and Storage of Folate

Mentor: Dr. H. Frederik Nijhout   Biology Department, Duke University

Tiffany J. Chen

Objectives:

- To estimate the average pool sizes of folate distributed within the plasma, the cell, and the mitochondria.
- To develop mathematical models that represent these pool sizes and mimic real bodily responses to day-to-day changes in diet and metabolism.
- To test these models against experimental data, as well as make predictions.

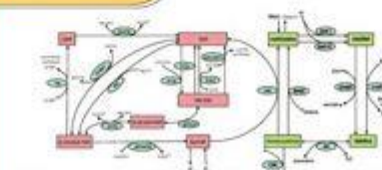

Figure 1.

Background:

Folate, or vitamin B9, is important for the synthesis of thymidine, a pyrimidine, and purines. Deficiency in folate is associated with megaloblastic anemia, cancer, cardiovascular disease, neurological disorders, and neural tube defects in infants. Folate metabolism provides the rate-limiting step for DNA synthesis and DNA and histone methylation (Fig. 1). Reduced folate status affects these critical cellular activities and also increases the level of homocysteine, a highly reactive amino acid that is associated with cell damage. It has been shown that increased folate intake by pregnant women can help reduce the risk of infant neural tube defects, presumably due to a reduction in plasma homocysteine levels. Folate metabolism occurs within cells, but their levels are typically measured in the plasma. It is therefore critical to understand the relationship between the concentrations of folate in the plasma and the cell.

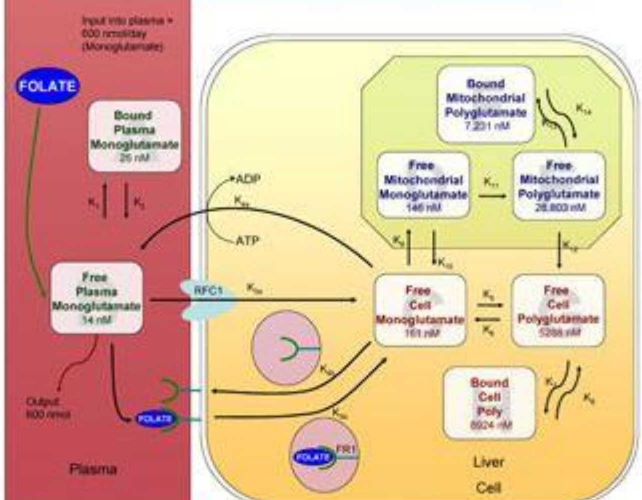

Figure 2.

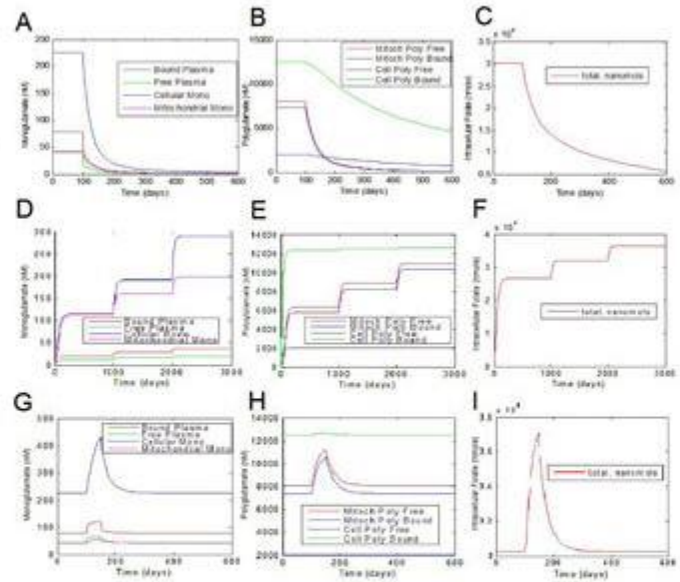

Figure 3

Methods:

Various pool values for plasma and intracellular folate were collected from experimental data (Figure 2). We made predictions for pool values that are not readily available. These predictions were based on known distribution of the various folate pools within the body. For example, 50% of body folate is stored in the liver – the liver contains 2 compartments. These are the cytosol and the mitochondria, each containing three general pools, monoglutamate, free polyglutamate, and bound polyglutamate. These individual pools have different proportions in the cytosol and the mitochondria.

After pool values were established, we assumed that transport of molecules between pools were based on first-order mass-action kinetics. We used Michaelis-Menten equations for the bound polyglutamate pools, because there is a limited amount of protein that will bind to folate – mainly glycine N-methyltransferase (GNMT), one of the enzymes in the methionine cycle (Fig. 1). In addition, we used Michaelis-Menten kinetics for the transport of folates in and out of the cell via Reduced Folate Carrier 1 (RFC1), Folate Receptor 1 (FR1), and an ATP-dependent exporter (Fig. 2).

Rate constants, or k-values, were calculated by assuming certain fluxes between pools. These fluxes were determined by known rates of gain and loss of folate in different compartments where these rates were known, and by adjusting the relative rates of input and output to obtain the right pool sizes between compartments in cases where the absolute rates were not known.

Experiments were performed by varying folate input. These were performed to determine half-lives of the pools, as well as to determine how the pools reacted to example experimental conditions from the literature.

Results:

1. The Model

The model correctly simulates the sizes of the folate pools in the various compartments, including the cytosol, the mitochondria and the fractions bound to proteins in those compartments.

2. Predicted half-life of folate.

After we removed the constant input of folate into the system, all pools diminished over time, some more quickly than others (Figures 3A, 3B). We can also see in figure 3C that the approximate half-life for total intracellular folate is 80 days, which is close to predicted values of around 80-100. Bound polyglutamate seems to decrease at a much slower rate than the other pools.

3. Reaching steady-state values.

The time for the total intracellular pools to reach steady-state typically ranged from 300 to 500 days, which corresponds well with data from the literature. Consistent with the idea that there is a correlation between intracellular folate pool size, polyglutamation, and protein binding, all types of polyglutamate pools do in fact take longer to reach a steady-state value (Figures 3D, 3E).

4. Response to pulsed folate input.

The input of folate was increased to 1000 nmol/day for 50 days. Model plasma levels were quick to rise and fall with the sudden changes, which predicts that free as well as loosely bound monoglutamates will react quickly to changes in folate intake (Fig. 3G). Out of the polyglutamate pools, the model predicts that both bound pools will take longer to return to steady-state, although the mitochondrial bound polyglutamate will take the longest of all of the pools (Fig. 3H).

Conclusions:

We have constructed a mathematical compartment model for folate that takes into account the different methods of transport, as well as retention in the plasma, cell, and mitochondria. We have compared the output of this model with results from current experiments, and have found that the model accurately simulates data from the literature. This model will for the foundation for future studies on the metabolism, transport and sequestration of folates under various genetic and environmental conditions.

Many thanks to Dr. H.F. Nijhout for his guidance and his patience, as well to both Dr. Nijhout and Dr. M.C. Reed for the use of their folate and methionine cycle programs and diagrams. Initial research was supported (in part) by a Howard Hughes Summer Research Fellowship.

SINGLE-PEDICLED FASCIOCUTANEOUS FLAP SURVIVAL IN AGED RAT MODEL OF CHRONIC ALCOHOLISM

Edita Aksamitiene, Ph.D.[1,2], Sudeep Roy, M.D.[1], Kealan Hobelmann, B.S.[1], Julianna Rodin B.A.[1], Giuseppe V. Staltari, B.S.[1], Edmund A. Pribitkin M.D.[1] and Joannes B. Hoek, Ph.D.[2],

[1] Department of Otolaryngology - Head & Neck Surgery, Thomas Jefferson University, Philadelphia, Pennsylvania 19107
[2] Department of Pathology, Anatomy & Cell Biology, Thomas Jefferson University, Philadelphia, Pennsylvania 19107

PROGRAM NO: 889.13
ABSTRACT NO: 8562

● INTRODUCTION ●

The use of pedicled skin flaps has significantly improved the safety and functional outcomes of surgery aimed at restoring function, form and integrity of craniofacial organs after traumatic injuries or resection of tumor [1]. Single-pedicled rotational flap remains attached to the donor site via an intact vascular pedicle, which serves as a conduit for supplying nutrients and removing waste from the flap during healing process.

Wound healing occurs through several overlapping but distinct stages: 1) hemostasis; 2) inflammation; 3) proliferation and 4) maturation. The 3rd stage occurs between 3-14 days after an injury, when the wound is 'rebuilt' with new granulation tissue. Different cell types migrate, proliferate and differentiate over an injured dermis. Many of them release angiogenic growth factors, such as VEGF, that trigger generation of new capillary blood vessels from the pre-existing vasculature to provide nutrients and oxygen to active cells with greatly increased metabolic demands [2, 3].

Various systemic factors, such as patient's old age, obesity, chronic diseases, smoking, stress etc., can prolong inflammatory phase of wound healing and impair angiogenesis [4]. Inadequate blood supply is the primary intrinsic factor affecting ischemic flap survival. In addition, under chronic hypoxic and inflammatory conditions, excessive ROS production, persistent presence of TGFβ and pro-inflammatory cytokines, such as IL-6, IL-1β and TNFα, result in enhanced synthesis and proteolytic activity of matrix metalloproteinases (MMPs) [5, 6]. Highly degradative environment, which decreases formation of granulation tissue, fibroblast proliferation and collagen production, compromises cutaneous tissue repair and predisposes a flap to ischemic necrosis. Skin flap failure remains a significant clinical problem in surgery, which should be overcome by understanding the molecular mechanisms underlying successful flap integration [7].

◆ GOAL OF STUDY ◆

Both acute and chronic ethanol intake increases ROS generation [8], but it may differently modulate immune cell activation and cytokine production that in turn may improve or delay wound healing [9-11]. Here we aimed to determine if there is a statistically significant correlation between chronic alcohol-induced changes at the cellular and molecular level in aged skin and a fate of single-pedicled composite (fasciocutaneous) flap.

❖ EXPERIMENTAL MODEL OF ISCHEMIC FLAP ❖

Impact of chronic alcohol intake on composite flap survival and underlying signaling events was examined in isocaloric pair-fed >1 year old Sprague-Dawley rats that consumed Lieber-DeCarli '82 liquid 1000 kcal/L diet consisting of 15.1% protein, 35.9% fat and either 49% carbohydrates (control group) or 13.5% carbohydrates and 35.5% ethanol (alcoholic group). Ten pairs of rats that were fed such diet for at least one year underwent surgery, where a 3:8 cm width to length ratio pedicled fasciocutaneous flap based on the inferior epigastric artery was raised in each anaesthetized rat and then rotated 60° degrees into a "defect" site that was created in the ventral surface (Fig. 1A-C). Whole piece of skin excised from a defect site on day 0 was used as control for protein basal levels (W).

In addition, four sterile polyvinyl alcohol (PVA) sponges were placed in different locations under the laid flap. On post-operative day (POD) 9 (end-point) the remaining sutures were removed, an entire flap was harvested, the PVA sponges were excised and placed in the lysis buffer containing protease and phosphatase inhibitors. The animal was subsequently euthanized in CO_2 chamber. Each flap was photopgraphed under standardized conditions, separated into proximal (P), middle (M) and distal (D) thirds (segments) (Fig. 1D), and snap frozen. For protein analysis, the flap segments were individually crushed into fine powder under liquid nitrogen, and then homogenized using Potter-Elvehjem Grinding Chambers in a modified RIPA tissue lysis buffer (see Box). Protein expression was analyzed by comparative Multi-strip Western blotting (MSWB) in LDS-PAGE system [12].

❖ 50 mM HEPES (pH. 7.4)	❖ 0.5 % Sodium deoxycholate
❖ 150 mM NaCl v	❖ 0.1 % SDS
❖ 1 % Triton X-100	❖ 70 mM n-Octyl-beta-D-Glucoside
❖ 1 mM EGTA	❖ Protease inhibitor cocktail III (A.G. Scientific)
❖ 10 % Glycerol	❖ Phosphatase inhibitor cocktail (Roche)

Protein transfer conditions:
❖ 4-12% gradient gel
❖ XCell II™ Blot Module
❖ 30 V constant
❖ 1 hour 30 min

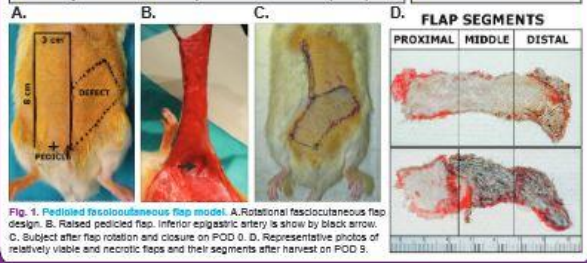

Fig. 1. Pedicled fasciocutaneous flap model. A.Rotational fasciocutaneous flap design. B. Raised pedicled flap. Inferior epigastric artery is show by black arrow. C. Subject after flap rotation and closure on POD 0. D. Representative photos of relatively viable and necrotic flaps and their segments after harvest on POD 9.

⌘ RESULTS: Flap survival ⌘

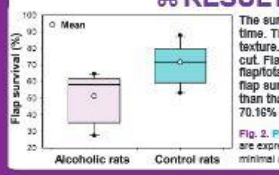

The survival areas of the flaps were clearly demarcated within 9 days time. The surviving skin was pink-white, tender, and normal in its texture. The necrotic skin was black, rigid, dry, and did not bleed when cut. Flap survival was determined as percentage of the non-necrotic flap/total flap area in mm² (Fig. 2). Based on planimetric analysis, mean flap survival of rats that were fed alcohol diet was significantly lower than that of control rats - 51.21% ± 4.50% SEM (standard error) versus 70.16% ± 3.57% SEM (P = 0.004, t-test assuming equal variance).

Fig. 2. Percentage of flap survival in experimental animal groups. The results are expressed in box plots as mean ± SD (standard deviation), median (black line), minimal and maximal values (black circles) for each group (n = 9 per group).

⌘ RESULTS: Histology and IHC of flaps ⌘

Specimens from each segment harvested on POD 9 were put into 10% PBS-buffered formalin, fixed for 24 hours, embedded in paraffin and stained with Masson's Trichrome, H&E or antibodies against endothelial cell marker CD31. The acellular areas were pink and negative for hematoxylin-positive nuclei. Segment necrosis was considered to be full-thickness when involved epidermis, adnexal structures of dermis and subcutaneous adipose tissue (Fig. 3). Inflammatory infiltrate in flaps' fascia contained neutrophils, monocytes and sparse macrophages.

GT - granulation tissue; SC - scab; E- epithelium; SF - subcutaneous fat; PC - panniculus carnosus (muscle layer in superficial fascia); D - dermis;	KEY colors in Masson's Trichrome (MT) staining: ❖ BRIGHT RED - cytoplasm, muscle, erythrocytes, keratin ❖ DARK PURPLE - cell nuclei; ❖ BLUE - collagen fibers

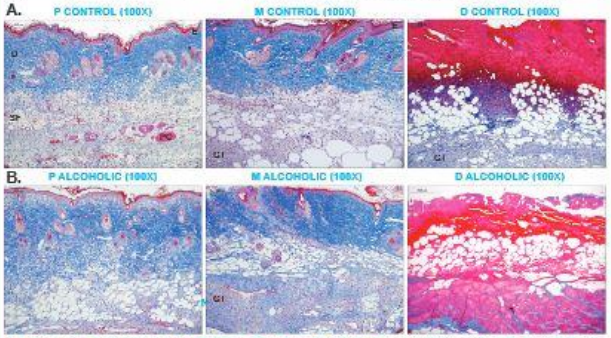

Fig. 3. Low-power photomicrographs of MT stained longitudinal sections of representative proximal (P), middle (M) and distal (D) flap segment specimens from control (A) and alcoholic (B) animal groups. Majority of D segments of control rats showed some degreee of cellularity, whereas most alcoholic rat specimens demonstrated full-thickness acellular necrosis.

⌘ RESULTS: Protein analysis ⌘

First, certain protein markers (see box below) were detected by immunoblotting (IB) in different flap segments to see how their expression reflects the severity of visible necrosis (Fig. 4A). Then the levels of these proteins were compared in control and alcoholic animal pairs separately (Fig. 4B). Finally, an expression of selected proteins in a given flap segment was simultaneously detected in the lysates of every rat pair by using MSWB (Fig. 4C). Protein signal intensities were calculated, normalized and plotted (Figs. 4, 5).

❖ Cleaved (CL) Caspase-9 - apoptosis; ❖ p-Akt (S473) & p-STAT3 (Y705) - cell survival;
❖ Src family kinases (SFK) (Y416) & Hsp27 - wound contraction; ❖ TGFβ & PAI - 1 - fibrosis and apoptosis;
❖ p-ERK1/2 (T202/Y204) - cell proliferation; ❖ p-PLC-γ (S1248) & p-p38 MAPK (T180/Y182)- cell motility;
❖ p-JNK1 (p46) (T183/Y185) - TNFα-induced cell death [13-14]; ❖ IL-1β & TNFα - tissue inflammation and death;
❖ VEGF & FGF-2 - angiogenesis; ❖ CD144 (Vascular endothelial (VE) Cadherin) - vascularity
❖ MMP-9 (produced by activated neutrophils & macrophages) - ECM, including viable and non viable collagen degradation; marker of chronic wound and inflammation;
❖ α-SMA - marker of vascular smooth muscle cells and of fibroblast differentiation into myofibroblasts;
❖ Collagen type I - deposited by fibroblasts; marker of wound healing.

⌘ RESULTS: Protein analysis ⌘

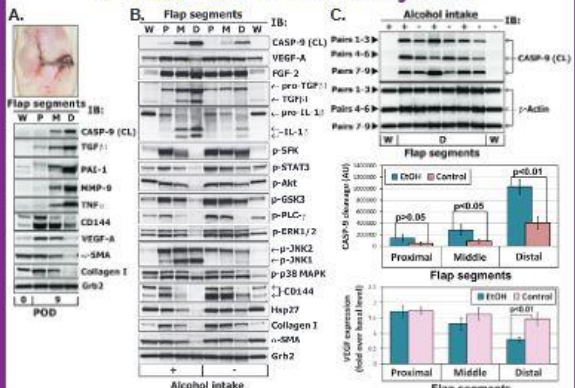

Fig. 4. A. Correlation between the severity of flap failure and the expression of protein markers in healthy (W) skin prior to wounding and proximal (P), middle (M) or distal (D) flap segments at 9th day after raising flap. B. Comparison of protein expression in flap segments of control and alcoholic paired rats. Representative 1 pair with flap survival rates of 73.44% (alcohol intake -) and 36.61% (alcohol intake +) is shown. W - basal conditions. C. Caspase-9 cleavage under basal (W) conditions and in distal flap segments of alcoholic and control rats at POD 9. D. VEGF-A levels under basal (W) conditions and in different flap segments of alcoholic and control rats at POD 9.

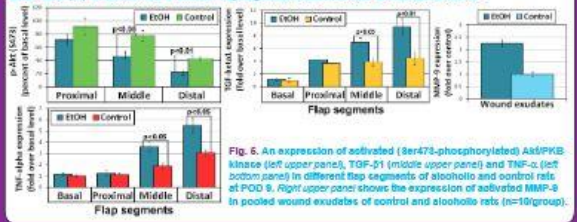

Fig. 6. An expression of activated (Ser473-phosphorylated) Akt/PKB kinase (left upper panel), TGF-β1 (middle upper panel) and TNF-α (left bottom panel) in different flap segments of alcoholic and control rats at POD 9. Right upper panel shows the expression of activated MMP-9 in pooled wound exudates of control and alcoholic rats (n=10/group).

■ CONCLUSION ■

Chronic alcohol consumption sustains cellular production of pro-inflammatory cytokines, inhibits the anti-apoptotic PI3-kinase/Akt signaling, augments activated MMP-9 levels in wound exudates by 2.25-fold and significantly decreases single-pedicled fasciocutaneous rotational flap survival in aged rats.

ACKNOWLEDGEMENTS

This research was supported by Thomas Jefferson University Department of Otolaryngology - Head & Neck Surgery.

PRESENTER: Edita Aksamitiene, PhD
Edita.Aksamitiene@jefferson.edu
THANK YOU for your time!

♦ REFERENCES ♦

1. Honrado, CP et al. Facial Plast Surg Clin N Am 13 (2005) 203–214
2. Velnar, T et al. J Int Med Res. 2009; 37: 1528 – 1542
3. Bao, P et al., J Surg Res. 2009 May 15; 153(2): 347–358
4. Guo, S & DiPietro, L.A. J Dent Res. 2010 Mar; 89(3): 219–229.
5. Eming, SA et al. Sci Transl Med 3 2014; 5(205): p. 205rv6
6. Han, YP et al., J Biol Chem. 2001; 276:22341–50
7. Baker, SR. Local Flaps in Facial Reconstruction. Elsevier 2007;
8. Sid, B., et al. Free Radical Research, 2013; 47(11): 894–904
9. Mendelsker, P et al., J Immunol 2009; 183:1320–1327
10. Watson, RR. Alcohol, Drugs of Abuse, and Immune Functions
11. Aksamitiene E, et al. Electrophoresis. 2007 Sep;28(18):3152-73.
12. Klyatkin & Aksamitiene. Methods Mol Biol. 2009; 536: 149–161
13. Liu, Jet al., Mol Cell Bio. 2004 24(24): 10844-56
14. Chen, EC. PNAS, 1997; 94(24): 13169–13174

Epigenetic Mediated Early Induction of Adipocyte Differentiation Contributes to Programmed Obesity in Intrauterine Growth Restricted Newborns

[1]Mina Desai, Ph.D., [2]Robert H. Lane, M.D., [1]Guang Han, M.D., [1]Thomas R. Magee, Ph.D., and [1]Michael G. Ross, M.D., M.P.H.
[1]Dept. of Obstetrics and Gynecology, Harbor-UCLA Medical Center (LABioMed), Torrance, California; [2]Dept. of Neonatology, University of Utah, Salt Lake

ABSTRACT

OBJECTIVE: A key feature of gestationally programmed obesity in intrauterine growth restricted (IUGR) newborns is enhanced adipogenesis. Adipogenesis is driven by adipocyte differentiation, a process whereby previously silent adipogenic genes are activated, in part, via epigenetic mechanisms. DNA methyltransferase (DNMT3a) and histone deacetylase (HDAC1) both suppress gene expression. We have previously shown that maternal food restriction results in IUGR newborns that develop adult obesity. Notably at 1 day of age, IUGR newborns have upregulated expression of adipogenic transcription factors (PPARγ, C/EBPα). We hypothesized that IUGR adipocytes exhibit enhanced adipocyte differentiation as a result of epigenetic mediated enhanced induction of adipogenic genes. Using primary adipocyte cultures, we determined the degree of induction of epigenetic modulators, adipogenic transcription factors and their downstream lipogenic target genes (SREBP1, fatty acid synthase, acetyl-CoA carboxylase) in IUGR and Control offspring.

METHODS: Control dams received ad libitum food, whereas study dams were 50% food-restricted from pregnancy day 10 to term, resulting in IUGR newborns. Adipose tissue was obtained from 1 day old IUGR and Control newborns and cultured for 48h (time 0), at which time cells were induced to differentiate. Protein was extracted at day 0, 2, 4 and 6 and expression of epigenetic (DNMT3a, HDAC1), adipogenic (PPARγ, C/EBPα), and lipogenic factors (SREBP1, fatty acid synthase, acetyl-CoA carboxylase) were determined. Values were normalized to GAPDH and presented as fold change.

RESULTS: In IUGR and Control adipocytes, prior to induction at day 0, DNMT3a and HDAC1 were highly expressed, in association with absent expression of adipogenic and lipogenic factors. With induction, IUGR DNMT3a and HDAC1 decreased by 90%, while Control DNMT3a and HDAC1 decreased minimally (30-40%). IUGR demonstrated greater expression of adipogenic (PPARγ 2.5 vs 1.8 fold) and lipogenic genes (SREBP1 2.2 vs 1.8 fold), which also occurred earlier in IUGR (peak value at 4 day) as compared to Controls (peak value at 6 day).

CONCLUSION: Enhanced induction of adipogenic genes as a result of highly suppressible DNMT3a and HDAC1 likely contributes to increased adipogenesis and obesity in IUGR offspring.

BACKGROUND & OBJECTIVES

- Adipogenesis is induced by pre-adipocyte differentiation and adipocyte proliferation with concomitant induction of adipogenic transcription factor. PPARγ, followed by activation of lipogenic transcription factor, SREBP1. The activation of previously silent genes is regulated in part by epigenetic mechanisms.
- Despite low birth weight, intrauterine growth restricted (IUGR) newborns have a programmed predisposition to adult obesity. Suggesting an enhanced adipogenesis, IUGR newborns have upregulated expression of adipogenic transcription factor (PPARγ).
- DNA methyltransferase (DNMT3a) and histone deacetylase (HDAC1) both suppress gene expression (Figure 1). DNMT3a is responsible for methylation of genes during embryonic development and cell differentiation. HDAC1 deacetylates histones and thus suppresses gene transcription.
- We hypothesized that IUGR adipocytes exhibit enhanced adipocyte differentiation as a result of epigenetic mediated enhanced induction of adipogenic genes. Using primary adipocyte cultures, we determined the degree of induction of epigenetic modulators, adipogenic transcription factors and their downstream lipogenic target genes (SREBP1, fatty acid synthase, acetyl-CoA carboxylase) in IUGR and Control offspring.

METHODS

Newborn (p1) Primary Adipocyte Cultures

- **Study Groups:** Control dams received ad libitum food, whereas study dams were 50% food-restricted from pregnancy day 10 to 21 to produce IUGR newborns.
- **Adipocyte Cultures:** Adipose tissue was obtained from 1 day old IUGR and Control newborns and isolated pre-adipocytes were cultured in DMEM media supplemented with 10% FBS and 1% Antibiotic-Antimycotics. At 48h of culture (time 0), cells were induced to differentiate using dexamethasone (1μM), methylisobutylxanthine (0.1 mM), and insulin (10 μg/ml) (Figure 2) and samples collected at 2, 4, and 6 days.
- **Protein Expression:** Protein was extracted from all samples and expression determined (Western Blot) of epigenetic modulators (DNMT3a; HDAC1), adipogenic transcription factor (PPARγ) and the downstream lipogenic target genes (SREBP1, fatty acid synthase, acetyl-CoA carboxylase). Protein expression was normalized to GAPDH and values are means ± SE.

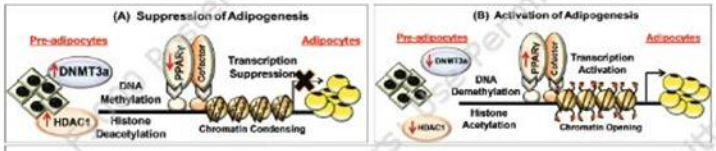

Figure 1. Epigenetic Regulation of Adipocyte Differentiation
(A) Suppression of Adipogenesis: Increased DNMT3a (methylation) and increased HDAC1 (deacetylation) silences adipogenic gene PPARγ and hence prevents pre-adipocytes differentiation to adipocytes.
(B) Activation of Adipogenesis: Decreased DNMT3a (demethylation) and decreased HDAC1 (acetylation) increases transcription of adipogenic gene, PPARγ and hence induces pre-adipocyte differentiation to adipocytes

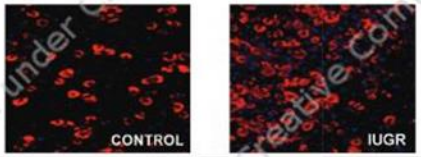

Figure 2. Images of Adipocyte Differentiation
Control and IUGR pre-adipocytes were cultured in differentiation media over 6 days and stained with Oil-O-Red (lipid and differentiation marker, red) and DAPI (nuclei, blue). IUGR has markedly increased number of differentiated adipocytes.

RESULTS

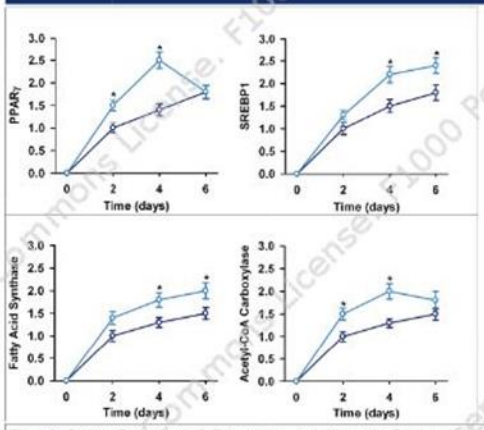

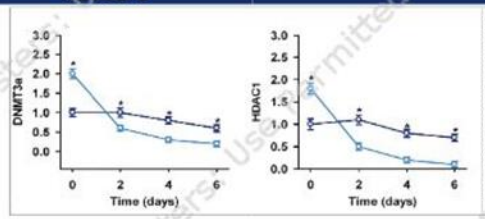

Figure 3. Protein Expression of Transcription and Lipogenic Factors during Adipocyte Differentiation
Control (●) and IUGR (○) pre-adipocytes were cultured in differentiation media over 6 days. Values are mean ± SE. *P<0.05 vs. Control. (1) IUGR adipocytes demonstrated markedly increased adipogenic (PPARγ) and lipogenic (SREBP1) transcription factors, in association with increased lipid enzymes (fatty acid synthase and acetyl-coA carboxylase) during adipocyte differentiation. (2) Both Control and IUGR pre-adipocytes do not express PPARγ, SREBP and lipid enzymes. (3) IUGR show earlier peak (4 days) as compared to Control (6 days) adipocytes.

Figure 4. Expression of Epigenetic Factors during Adipocyte Differentiation
Control (●) and IUGR (○) pre-adipocytes were cultured in differentiation media over 6 days. Values are mean ± SE. *P<0.05 vs. Control. (1) IUGR adipocytes demonstrated markedly increased basal levels of DNMT3a and HDAC1 which were markedly suppressed in response to culture in differentiation media. (2) Both Control and IUGR pre-adipocytes had higher levels of DNMT3a and HDAC1 as compared to differentiated adipocytes.

CONCLUSION

- Pre-adipocytes do not express adipose tissue transcription factors or lipogenic enzymes prior to differentiation.
- Increased basal levels of epigenetic factors in IUGR pre-adipocytes suggests a suppression of gene transcription.
- With induction of differentiation, IUGR adipocytes demonstrate a marked reduction of epigenetic silencing factors and an increase in adipogenic transcription factors and lipogenic enzymes.

These results suggest a programmed increased potential for enhanced adipogenesis in IUGR offspring, independent of the body hormonal milieu or offspring diet.

ACKNOWLEDGEMENTS

Grant Funding: M.D. is supported by 5R01DK081756 NIH/NIDDK and M.G.R. is supported by 5R01HD054751 NIH/NICHD.

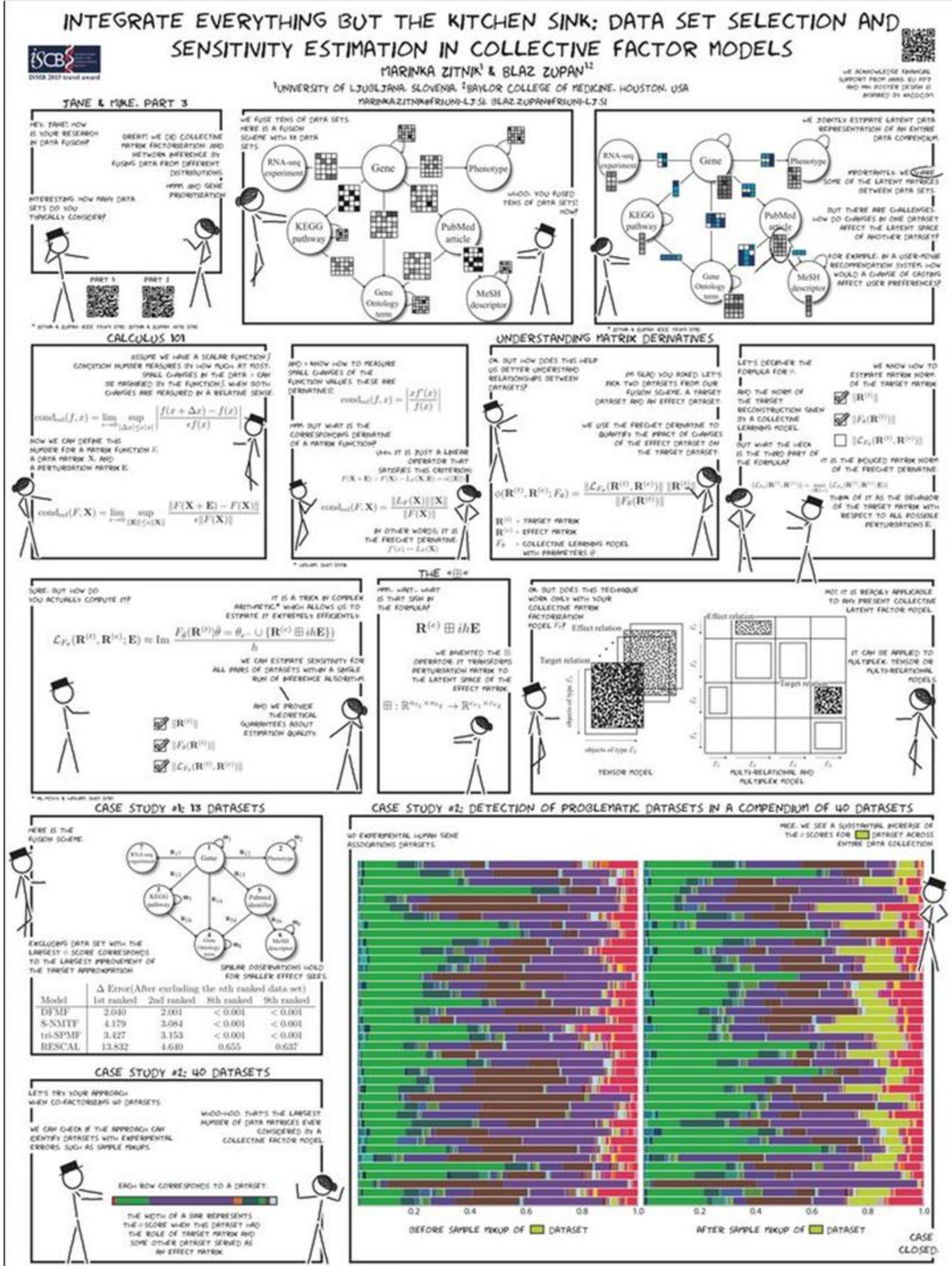

INTEGRATE EVERYTHING BUT THE KITCHEN SINK: DATA SET SELECTION AND SENSITIVITY ESTIMATION IN COLLECTIVE FACTOR MODELS
MARINKA ZITNIK[1] & BLAZ ZUPAN[1,2]
[1]UNIVERSITY OF LJUBLJANA, SLOVENIA [2]BAYLOR COLLEGE OF MEDICINE, HOUSTON, USA
MARINKA.ZITNIK@FRI.UNI-LJ.SI, BLAZ.ZUPAN@FRI.UNI-LJ.SI
ISCB
WE ACKNOWLEDGE FINANCIAL SUPPORT FROM ARRS, EU FP7 AND NIH. POSTER DESIGN IS INSPIRED BY XKCD.COM.
JANE & MIKE, PART 3
HEY, JANE! HOW IS YOUR RESEARCH IN DATA FUSION?
GREAT! WE DID COLLECTIVE MATRIX FACTORIZATION AND NETWORK INFERENCE BY FUSING DATA FROM DIFFERENT DISTRIBUTIONS.
HMM, AND GENE PRIORITIZATION.
INTERESTING. HOW MANY DATA SETS DO YOU TYPICALLY CONSIDER?
PART 1
PART 2
WE FUSE TENS OF DATA SETS. HERE IS A FUSION SCHEME WITH 18 DATA SETS.
RNA-seq experiment
Gene
Phenotype
KEGG pathway
PubMed article
Gene Ontology term
MeSH descriptor
WHOO, YOU FUSED TENS OF DATA SETS! HOW?
WE JOINTLY ESTIMATE LATENT DATA REPRESENTATION OF AN ENTIRE DATA COMPENDIUM.
IMPORTANTLY, WE SHARE SOME OF THE LATENT MATRICES BETWEEN DATA SETS.
BUT THERE ARE CHALLENGES: HOW DO CHANGES IN ONE DATASET AFFECT THE LATENT SPACE OF ANOTHER DATASET?
FOR EXAMPLE, IN A USER-MOVIE RECOMMENDATION SYSTEM, HOW WOULD A CHANGE OF CASTING AFFECT USER PREFERENCES?
CALCULUS 101
ASSUME WE HAVE A SCALAR FUNCTION f. CONDITION NUMBER MEASURES BY HOW MUCH AT MOST SMALL CHANGES IN THE DATA x CAN BE MAGNIFIED BY THE FUNCTION f, WHEN BOTH CHANGES ARE MEASURED IN A RELATIVE SENSE.
$\mathrm{cond}_{rel}(f,x) = \lim_{\epsilon \to 0} \sup_{|\Delta x| \leq \epsilon |x|} \left| \frac{f(x+\Delta x) - f(x)}{\epsilon f(x)} \right|$
NOW WE CAN DEFINE THIS NUMBER FOR A MATRIX FUNCTION F, A DATA MATRIX X, AND A PERTURBATION MATRIX E.
$\mathrm{cond}_{rel}(F,\mathbf{X}) = \lim_{\epsilon \to 0} \sup_{\|\mathbf{E}\| \leq \epsilon \|\mathbf{X}\|} \frac{\|F(\mathbf{X}+\mathbf{E}) - F(\mathbf{X})\|}{\epsilon \|F(\mathbf{X})\|}$
AND I KNOW HOW TO MEASURE SMALL CHANGES OF THE FUNCTION VALUES. THESE ARE DERIVATIVES!
$\mathrm{cond}_{rel}(f,x) = \left| \frac{x f'(x)}{f(x)} \right|$
HMM, BUT WHAT IS THE CORRESPONDING DERIVATIVE OF A MATRIX FUNCTION?
UHH, IT IS JUST A LINEAR OPERATOR THAT SATISFIES THIS CRITERION:
$\mathrm{cond}_{rel}(F,\mathbf{X}) = \frac{\|L_F(\mathbf{X})\| \|\mathbf{X}\|}{\|F(\mathbf{X})\|}$
IN OTHER WORDS, IT IS THE FRECHET DERIVATIVE.
$f'(x) = L_F(\mathbf{X})$
UNDERSTANDING MATRIX DERIVATIVES
OK, BUT HOW DOES THIS HELP US BETTER UNDERSTAND RELATIONSHIPS BETWEEN DATASETS?
I'M GLAD YOU ASKED. LET'S PICK TWO DATASETS FROM OUR FUSION SCHEME, A TARGET DATASET AND AN EFFECT DATASET.
WE USE THE FRECHET DERIVATIVE TO QUANTIFY THE IMPACT OF CHANGES OF THE EFFECT DATASET ON THE TARGET DATASET.
$\phi(\mathbf{R}^{(t)}, \mathbf{R}^{(e)}; F_\theta) = \frac{\|\mathcal{L}_{F_\theta}(\mathbf{R}^{(t)}, \mathbf{R}^{(e)})\| \|\mathbf{R}^{(t)}\|}{\|F_\theta(\mathbf{R}^{(t)})\|}$
$\mathbf{R}^{(t)}$ = TARGET MATRIX
$\mathbf{R}^{(e)}$ = EFFECT MATRIX
F_θ = COLLECTIVE LEARNING MODEL WITH PARAMETERS θ
LET'S DECIPHER THE FORMULA FOR ϕ.
WE KNOW HOW TO ESTIMATE MATRIX NORM OF THE TARGET MATRIX
AND THE NORM OF THE TARGET RECONSTRUCTION GIVEN BY A COLLECTIVE LEARNING MODEL.
BUT WHAT THE HECK IS THE THIRD PART OF THE FORMULA?
IT IS THE INDUCED MATRIX NORM OF THE FRECHET DERIVATIVE.
THINK OF IT AS THE BEHAVIOR OF THE TARGET MATRIX WITH RESPECT TO ALL POSSIBLE PERTURBATIONS E.
SURE. BUT HOW DO YOU ACTUALLY COMPUTE IT?
IT IS A TRICK IN COMPLEX ARITHMETIC* WHICH ALLOWS US TO ESTIMATE IT EXTREMELY EFFICIENTLY.
$\mathcal{L}_{F_\theta}(\mathbf{R}^{(t)}, \mathbf{R}^{(e)}; \mathbf{E}) \approx \mathrm{Im} \frac{F_{\hat{\theta}}(\mathbf{R}^{(t)} | \hat{\theta} = \theta_{e^-} \cup \{\mathbf{R}^{(e)} \boxplus ih\mathbf{E}\})}{h}$
WE CAN ESTIMATE SENSITIVITY FOR ALL PAIRS OF DATASETS WITHIN A SINGLE RUN OF INFERENCE ALGORITHM.
AND WE PROVIDE THEORETICAL GUARANTEES ABOUT ESTIMATION QUALITY.
THE "⊞"
HMM, WAIT... WHAT IS THAT SIGN IN THE FORMULA?
$\mathbf{R}^{(e)} \boxplus ih\mathbf{E}$
WE INVENTED THE ⊞ OPERATOR. IT TRANSFORMS PERTURBATION MATRIX TO THE LATENT SPACE OF THE EFFECT MATRIX.
OK, BUT DOES THIS TECHNIQUE WORK ONLY WITH YOUR COLLECTIVE MATRIX FACTORIZATION MODEL F?
NO! IT IS READILY APPLICABLE TO ANY PRESENT COLLECTIVE LATENT FACTOR MODEL.
IT CAN BE APPLIED TO MULTIPLEX, TENSOR OR MULTI-RELATIONAL MODELS.
Effect relation
Target relation
TENSOR MODEL
MULTI-RELATIONAL AND MULTIPLEX MODEL
CASE STUDY #1: 13 DATASETS
HERE IS THE FUSION SCHEME.
EXCLUDING DATA SET WITH THE LARGEST ϕ SCORE CORRESPONDS TO THE LARGEST IMPROVEMENT OF THE TARGET APPROXIMATION.
SIMILAR OBSERVATIONS HOLD FOR SMALLER EFFECT SIZES.
Δ Error(After excluding the nth ranked data set)
Model | 1st ranked | 2nd ranked | 8th ranked | 9th ranked
DFMF | 2.040 | 2.001 | < 0.001 | < 0.001
S-NMTF | 4.179 | 3.084 | < 0.001 | < 0.001
tri-SPMF | 3.427 | 3.153 | < 0.001 | < 0.001
RESCAL | 13.832 | 4.640 | 0.655 | 0.637
CASE STUDY #2: 40 DATASETS
LET'S TRY YOUR APPROACH WHEN CO-FACTORIZING 40 DATASETS.
WE CAN CHECK IF THE APPROACH CAN IDENTIFY DATASETS WITH EXPERIMENTAL ERRORS, SUCH AS SAMPLE MIXUPS.
WHOO-HOO. THAT'S THE LARGEST NUMBER OF DATA MATRICES EVER CONSIDERED BY A COLLECTIVE FACTOR MODEL.
EACH ROW CORRESPONDS TO A DATASET.
THE WIDTH OF A BAR REPRESENTS THE ϕ SCORE WHEN THIS DATASET HAD THE ROLE OF TARGET MATRIX AND SOME OTHER DATASET SERVED AS AN EFFECT MATRIX.
CASE STUDY #2: DETECTION OF PROBLEMATIC DATASETS IN A COMPENDIUM OF 40 DATASETS
40 EXPERIMENTAL HUMAN GENE ASSOCIATIONS DATASETS
NICE. WE SEE A SUBSTANTIAL INCREASE OF THE ϕ SCORES FOR DATASET ACROSS ENTIRE DATA COLLECTION.
0.2 0.4 0.6 0.8 1.0
BEFORE SAMPLE MIXUP OF DATASET
AFTER SAMPLE MIXUP OF DATASET
CASE CLOSED.

EXPERIENCE-DEPENDENT EPIGENOMIC REORGANIZATION

COREY DUKE, ANDREW KENNEDY, CRISTIN GAVIN, DAVID SWEATT, JEREMY DAY

Department of Neurobiology, Evelyn F. McKnight Brain Institute, University of Alabama at Birmingham

THE UNIVERSITY OF ALABAMA AT BIRMINGHAM
Department of Neurobiology

Introduction

The formation and maintenance of new memories requires transcription and translation of genetic material, and epigenetic mechanisms such as methylation and demethylation serve as powerful regulators of gene expression that are crucial to these processes. Moreover, aberrant DNA methylation has been identified in neurological and psychiatric disease states associated with impaired cognition, such as Alzheimer's disease, autism-spectrum disorders, schizophrenia, and drug addiction. Here, we've harnessed whole-genome sequencing tools to systematically characterize memory-related changes in gene expression and DNA methylation status following memory acquisition.

Methods

Results

24 hr Threat Learning Gene Ontology

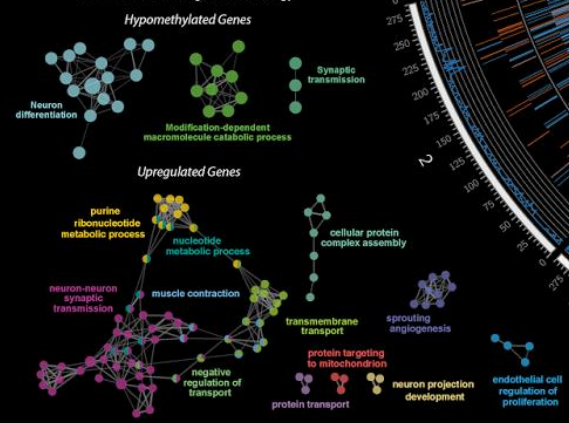

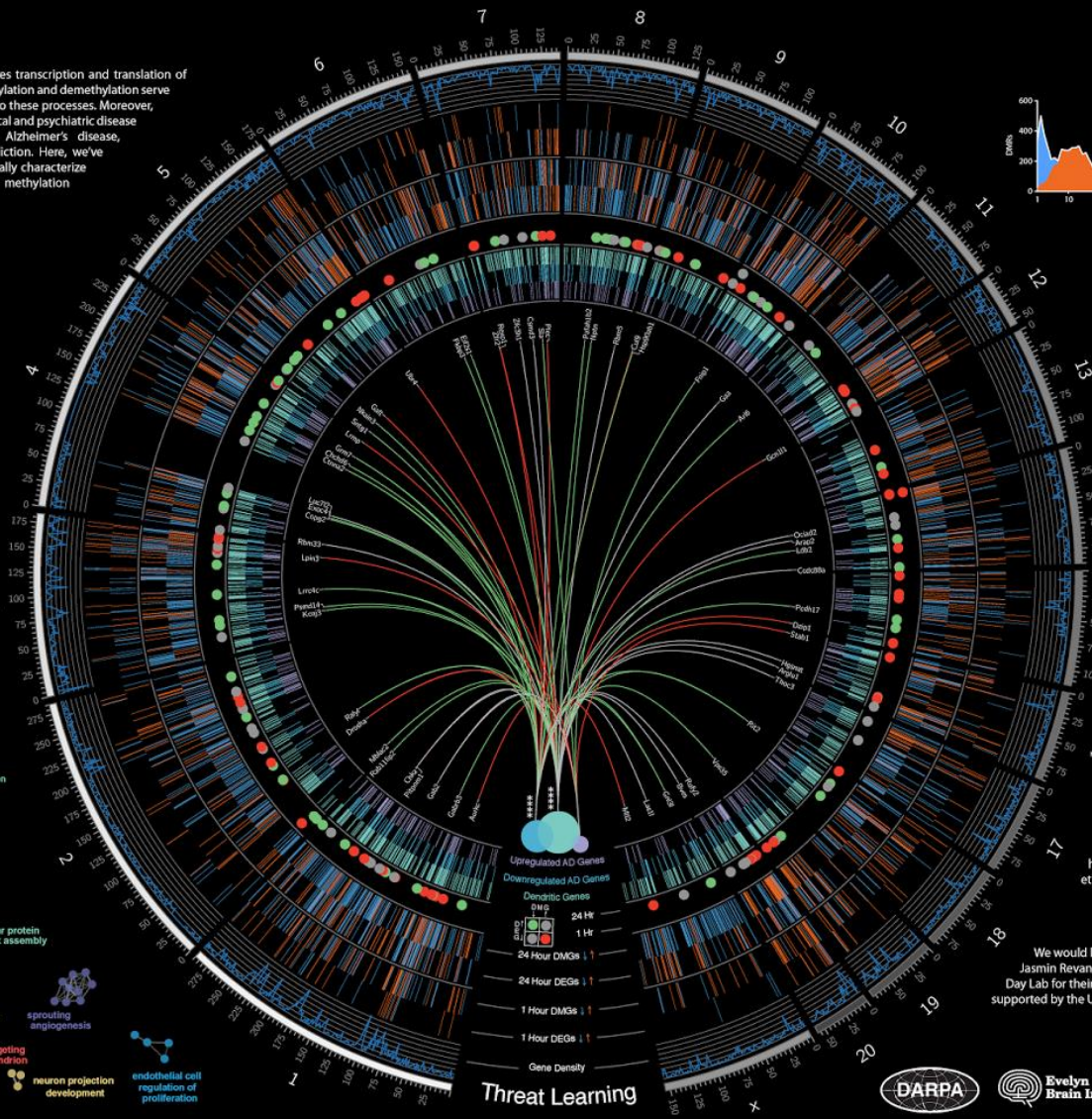

DNA Methylation Site Specificity

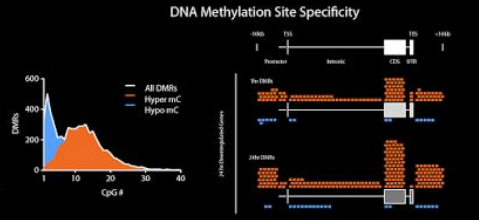

Individual Gene Profile

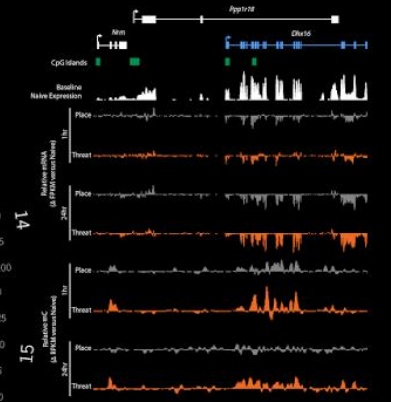

Conclusions/Future Work

Memory aquisition results in thousands of gene expression and epigenomic changes in the rat hippocampus that are experience dependent. These modifications are evident as early as one hour following the learning experience, and become more marked and pronounced after twenty four hours. Several of the coordinately upregulated and downregulated genes following a dramatic learning experience have been implicated in dendritic functions as wells as disease states. We hope to further explore the functional significance of these epigenetic marks, and to examine additional time points.

Acknowledgements

We would like to thank Svitlana Bach, Katherine Savell, Rhiana Simon, Jasmin Revanna, Faraz Sultan, Andrew Brane, and the other members of the Day Lab for their helpful discussions and comments. This research was partially supported by the UAB Medical Scientist Training Program.

Funding sources

DARPA
Evelyn F. McKnight Brain Institute
UAB MSTP
MSSRP THE UNIVERSITY OF ALABAMA AT BIRMINGHAM
NIDA NATIONAL INSTITUTE ON DRUG ABUSE

Morphological Correlates of Sidewinding Locomotion in Vipers

Jessica L. Tingle and Timothy E. Higham | University of California, Riverside
jessica.tingle@email.ucr.edu

Background

Most studies examining the relationship between habitat use and morphology in terrestrial vertebrates have focused on limbed locomotion (e.g. Moermond 1979; Losos 1990; Moen et al. 2013), despite the ecological diversity of some limbless taxa, particularly snakes. A few studies have uncovered body shape differences between arboreal and terrestrial snakes (Vitt and Vangilder 1983; Guyer and Donnelly 1990; Pizzatto et al. 2007; Alencar 2010). Another uncovered muscular differences in arboreal vs. terrestrial, aquatic, or burrowing species (Jayne 1982). Vipers provide the unique opportunity to examine the morphological differences between terrestrial generalists, arboreal specialists, and sand-dwelling species. In this study, we used recent advances in statistical methods and available phylogenies to rigorously examine ecomorphology in vipers.

Methods

We collected data on preserved specimens of 62 viper species.

Measured Variables

- Snout-vent length (SVL)
- Tail length
- Width and height at 25%, 50%, and 75% SVL
- Ventral scale count (correlated with vertebral count)

Calculated Shape Indices

- Elongation ratio (total length : width)
  - high = slender snake
  - low = stocky snake
- Relative tail length (percent of total length)
- Width : height
  - high = flattened body
  - low = laterally compressed body

Analysis

- Coded species as arboreal, sidewinding, or generalist (terrestrial, not specialized in sidewinding)
- Pruned phylogeny from Alencar et al. 2016, added some additional species
- Ran a size-corrected phylogenetic principal components analysis in R (Revell 2012)

Do vipers that specialize in different habitats differ in their morphology?

Arboreal Habitats

Challenge

Arboreal snakes must overcome gravity to bridge long gaps between branches.

Morphology

- Significantly different from terrestrial generalists on PC 1 and PC 2 ($p < 0.001$)
- Very slender (elongation ratio = 44 ± 11, vs. 3 ± 8)
- Laterally compressed (width : height = 0.7 ± 0.5 vs. 0.8 ± 0.1)
- Relatively long tails (17 ± 2% total body length, vs. 10 ± 3%)

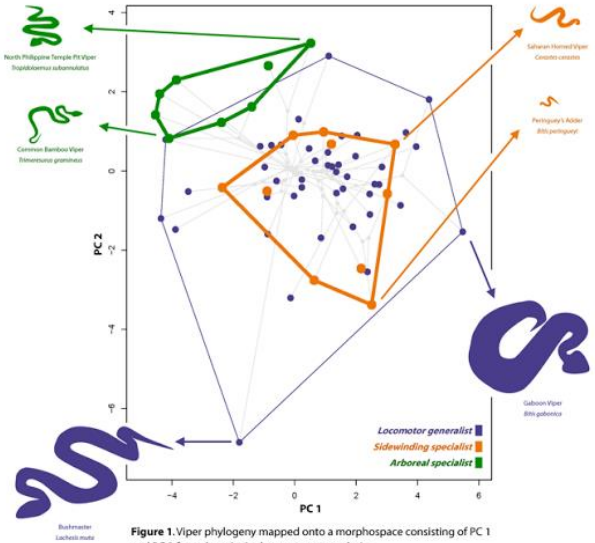

Figure 1. Viper phylogeny mapped onto a morphospace consisting of PC 1 and PC 2 from the principal components analysis.

Sandy Habitats

Challenge

Sand-dwelling snakes must overcome a shifting substrate.

Many sand-dwelling vipers move in a specialized way, called sidewinding. During sidewinding, the snake anchors one or more points of its body on the substrate while lifting an arc of its body forward until it can anchor a new point farther along.

Sidewinding Morphology

- Significantly less variance than terrestrial generalists on PC 2 ($p = 0.046$)
- Constrained
  - Never extremely large
  - Not extremely slender or stocky
  - No long tails (11% or less total body length)

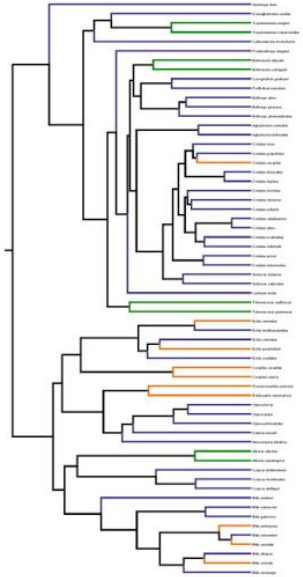

Figure 2. Viper phylogeny adapted from Alencar et al. 2016

Discussion

Arboreal vipers show morphological convergence with arboreal snakes in other clades (Pizzatto et al. 2007; Alencar 2010). Slender bodies might help snakes bridge longer gaps between branches, or to grip small branches more tightly. Lateral compression increases the area that snakes can use to push against the sides of branches or tree trunks. Long, prehensile tails help snakes grip branches more effectively.

Sidewinding vipers may be morphologically constrained because extreme morphologies impede sidewinding locomotion in some way. For example, it may be difficult for very large snakes to generate enough force to lift their bodies upward. Tails may not contribute to force generation during sidewinding, so very long tails may not be helpful to sidewinding specialists. Alternatively, morphological constraint may result from the harsh conditions of the desert rather than from locomotor specialization.

In the future, we will examine the link between morphology and biomechanics of sidewinding locomotion intra– and inter-specifically to quantify the effects that various aspects of morphology have on sidewinding.

Acknowledgements

- NSF Graduate Research Fellowships Program
- The Higham Lab, especially Vicky Zhuang
- Los Angeles County Museum of Natural History
- California Academy of Sciences
- UC Berkeley's Museum of Vertebrate Zoology
- San Diego Natural History Museum

Literature Cited

Alencar 2010. Ecomorphology in neotropical snakes: A study with the tribe Pseudoboini. *Masters thesis, Universidade de São Paulo.*

Alencar L.R.V., T.B. Quental, P.G. Grazziotin, M.L. Alves, M. Martins, M. Werneck, and H. Zaher. 2016. Diversification in vipers: Phylogenetic relationships, time of divergence and shifts in speciation rates. *Molecular Phylogenetics and Evolution* 105:50–62.

Guyer C. and M.A. Donnelly. 1990. Length-mass relationships among an assemblage of tropical snakes in Costa Rica. *Journal of Tropical Ecology* 6:65–76.

Jayne B.C. 1982. Comparative morphology of the semispinalis-spinalis muscle of snakes and correlations with locomotion and constriction. *Journal of Morphology* 172:83–96.

Lanza, L.B. 1990. The evolution of form and function: Morphology and locomotor performance in West Indian Anolis lizards. *Evolution* 44: 1180.

Moen, D.S., D.J. Irschick, and L.J. Wiens. 2013. Evolutionary conservatism and convergence both lead to striking similarity in ecology, morphology, and performance across continents in frogs. *Proceedings of the Royal Society B.*

Moermond T.C. 1979. Habitat constraints on the behavior, morphology, and community structure of Anolis lizards. *Ecology* 60:152–164.

Pizzatto L., G.A.B. Marques, and M. Martins. 2007. Ecomorphology of Boine snakes, with emphasis on South American forms. Pp. 51–68 in H.W. Henderson and R. Powell eds. Biology of the Boas and Pythons. Eagle Mountain Publishing LC, Eagle Mountain, Utah.

Revell, L.J. 2012. Phytools: An R package for phylogenetic comparative biology (and other things). *Methods in Ecology and Evolution* 3:217–223.

Vitt L.J. and L.D. Vangilder. 1983. Ecology of a snake community in northeastern Brazil. *Amphibia Reptilia* 4:273–296.

Jump locations of jump-diffusion with state-dependent rates

THE UNIVERSITY OF UTAH
Christopher E. Miles, James P. Keener
Department of Mathematics

Setup

X_t = Markov process with **two** (coupled) noise sources

jump process

characterized by: operator $\mathbb{J}$, rate $\lambda(X_t)$

fixed jump size: $X_{t_+} = X_{t_-} + \Delta$

$\mathbb{J}q := q(x - \Delta)$

fixed jump location: $X_{t_+} = \eta$

$\mathbb{J}q := \delta(x - \eta) \int_{-\infty}^{\infty} q(x,t)\,\mathrm{d}x$

diffusion process

characterized by: operator $\mathbb{L}$ (backward operator)

Itô diffusion: $\mathrm{d}Y_t = A(Y_t) + \sqrt{2D(Y_t)}\,\mathrm{d}W_t$

$\mathbb{L}q := \partial_y \{A(y)q\} + D(y)\partial_{yy}q$

Chapman-Kolmogorov equation

$$\partial_t \tilde{p}(x,t) = \mathbb{L}\tilde{p} - \lambda(x)\tilde{p} + \mathbb{J}\lambda\tilde{p}$$

$\tilde{p}(x,t)$ = density for X_t

Example

$\mathbb{L}p = \partial_x \{axp\} + Dp_{xx}$ $\quad \lambda = \alpha \exp\{-x^2/\beta\}$ $\quad \mathbb{J}p = p(x - \Delta)$

$\alpha = .1,\ D = 1,\ \alpha = 10,\ \beta = 10,\ \Delta = 1$

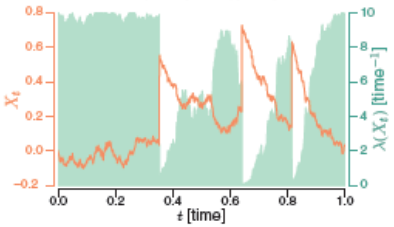

Jump Locations

$\{t_1, t_2, \ldots\}$:= jump times

focus of this work

*i*th jump location := X_{t_i}

other quantities of interest

$\tau_i := t_i - t_{i-1}$:= interjump times

Survival formulation

$$\begin{cases} \partial_t p(x,t) = \mathbb{L}p - \lambda p \\ \partial_t q(x,t) = \lambda p. \end{cases}$$

next jump location $p_j(x) = \int_0^{\infty} \lambda p\,\mathrm{d}t$

next jump time $p_\tau(t) = \int_{-\infty}^{\infty} \lambda p\,\mathrm{d}x$

Results

Theorem 1 $p_i(x)$:= distribution of *i*th jump location, satisfies

$$\begin{cases} \partial_t \hat{p}_i(x,t) = \mathbb{L}\hat{p}_i - \lambda\hat{p}_i \\ \hat{p}_i(x,0) = \mathbb{J}p_{i-1} \\ p_{i+1}(x) = \int_0^{\infty} \lambda\hat{p}_i\,\mathrm{d}t. \end{cases} \quad (1)$$

more convenient to study $u_i = p_i(x)/\lambda(x)$

Theorem 2 (1) is equivalent to the map

$$\mathbb{T}u_{i+1} = \mathbb{J}u_i \qquad \mathbb{T} := [\lambda(x) - \mathbb{L}]$$

importance

can construct sequence $\{u_1, u_2, \ldots\}$ and easily recover jump locations $\{p_1, p_2, \ldots\}$

Stationarity

Assuming X_t reaches stationarity

$p_\star$:= stationary jump distribution, $u_\star = p_\star/\lambda$

$\hat{p}_s$:= stationary distribution of full process

both satisfy

$$0 = \mathbb{L}u_\star - \lambda u_\star + \mathbb{J}\lambda u_\star, \qquad 0 = \mathbb{L}\hat{p}_s - \lambda\hat{p}_s + \mathbb{J}\lambda\hat{p}_s$$

explicit connection between jump locations and stationary density

but scaling is different $\int \hat{p}_s\,\mathrm{d}x = 1$, $\int u_\star\lambda\,\mathrm{d}x = 1$ — consequence

Theorem 3 stationary distribution $\hat{p}_s = p_\star$ jump location distribution

iff

$\lambda(x) = \lambda_0$

(no state dependence)

Interjump Times

Assuming jump locations $\{p_1, p_2, \ldots\}$ known from previous results

Mean interjump time $\langle \tau_i \rangle = \int_{-\infty}^{\infty} u_i\,\mathrm{d}x$

higher order moments satisfy more complicated (but tractable) differential relationships

Applications

Neuronal Integrate-and-fire

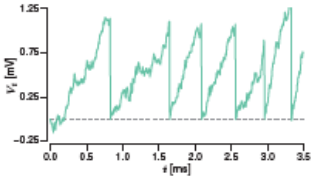

$\mathbb{L}p = -\partial_v \{\alpha p\} + Dp_{vv}$

$\lambda(v) = \gamma e^{v/\beta}$

$\mathbb{J}p = \delta(v) \int_{-\infty}^{\infty} p\,\mathrm{d}v$

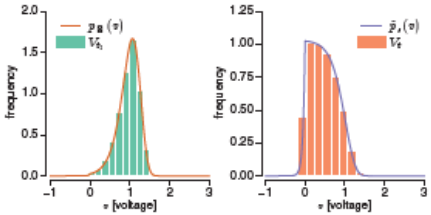

conclusion sharp firing threshold appears as a consequence of stochasticity from state-dependent rate

Molecular Motors?

$\lambda = \alpha \exp\{-x^2/\beta\}$

$\mathbb{L}p = \partial_x \{axp\} + Dp_{xx}$, $\mathbb{J}p = p(x - \Delta)$

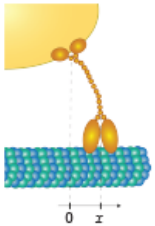

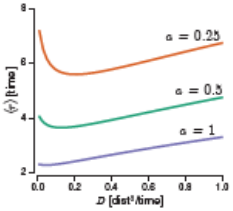

conclusion diffusion may have a non-monotonic effect on motor stepping rate

Future Work

use map formulation to study convergence to stationarity

find more applications (finance?)

relate to state-dependent switched systems (stochastic hybrid systems)

5/15/17

Digital ~~Demotic~~ DEMONIC

Codifying the evilest script in history

Christian Casey

The Problem

The Demotic script is pathologically complex. Changes over time and differences between scribal hands mean that it is impossible to identify a single, unified Demotic.

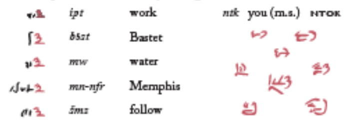

1) Different meaning, same shape   2) Same meaning, different shape

Previous Attempts

Nevertheless, the advantages of encoding Demotic for education and research purposes cannot be overstated. Many talented scholars have tried to bring order to this complex script, with the first work beginning in the 19th century. To this day, no one has succeeding in creating a version of Demotic that can be used by computers to store data.

An early attempt to typeset Demotic (Brugsch, 1860)
pȝ sḫ-šʿt jrm nȝ mt-rmṯ-kmy = (roughly) "The Demotic script and the Egyptians"

Encoding

The crucial task is to create an *encoding* – a mapping between the individual signs and a set of arbitrary numbers. An encoding allows texts to be stored and manipulated by computers. Encodings have been created sucessfully for other Egyptian scripts, such as Hieroglyphic and Coptic.

Excerpt from the Unicode Code Block for Egyptian Hierolgyphs

Proposed Solution

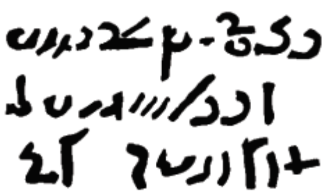

1) A monochrome facsimile of a Demotic text is prepared as input. This example uses a small sample text, but the final version uses several complete texts, which together span the entire history of the Demotic script (see "Selected Texts" below).

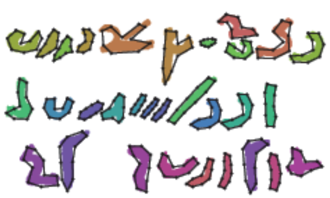

2) Connected shapes (blobs) are identified, and each is assigned an arbitrary integer label (here represented by different colors).
3) Blob outlines are precisely traced as high-dimensional polygons.
4) These polygons are interpolated to produce lower-dimensional polygons of a common order (10 points per blob in the above example).

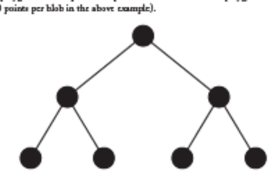

5) A hierarchical clustering algorithm identifies groups of physically similar signs.
6) The parameters to the algorithm revised to produce better clusters.
7) Individual clusters become a single code point in the final encoding.

Top: The Demotic portion of the Rosetta Stone with signs color coded according to cluster. Most glyphs are red because the largest cluster groups many different shapes together.
Bottom: Some example clusters with glyphs shown overlapping. This demonstrates the validity of the assumption that clusters correspond to glyph shape in an obvious and straightforward manner.

Typography

An encoding requires a typeface in order to be displayed. There are at least two possible methods for creating one.

Combining several instances of a sign creates a single, idealized form, but inscriptions offer the best source material for creating a typeface.

Input Method

Along with the font, an encoding also requires an input method. There are many approaches to this problem, but the simplest is to let the user draw signs with a tablet and programmatically select the best match.

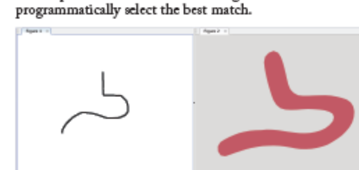

Input (left) and output (right) of an input method prototype.

Selected Texts

Timeline of Egyptian Languages and Scripts

Brown University

Thank you to the Brown Department of Egyptology and Assyriology for supporting my research and this poster session, and special thanks to Kurstyn Casey-Morrow for the drawing of Ammit.

Functional Peptide β-sheets Microsponges

Steven Harris Wibowo, Dr. Adrian Sulistio, Dr. Edgar H. H. Wong, Dr. Anton Blencowe, Prof. Greg G. Qiao*

Polymer Science Group, Department of Chemical and Biomolecular Engineering, The University of Melbourne,VIC 3010, Australia

stevenhw@student.unimelb.edu.au; *greggqh@.unimelb.edu.au

1. Introduction

Polypeptides have attracted widespread attention as building block of complex materials due to their ability to form higher-ordered structures such as β-sheets.[1,2] Still, the propensity of β-sheet-forming peptides to form unprocessable aggregates in solution remains a critical issue towards the preparation of well-defined β-sheet-assembled materials.

By employing surface-initiated N-carboxyanhydride ring-opening polymerization (SI-ROP), we recently reported a robust strategy to form well-defined peptide β-sheet architectures with sponge-like morphology. Herein, we demonstrate the unique ability of the H-bonded microsponges in entrapping metal nanoparticles, proteins, drug molecules and bio-relevant polymers via non-covalent interactions. This ability mimics the absorption/filtering ability of marine animals (e.g., sea sponges) and present a simple yet versatile approach towards the fabrication of functional materials for various applications.

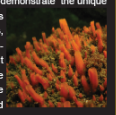

2. Synthetic Strategy

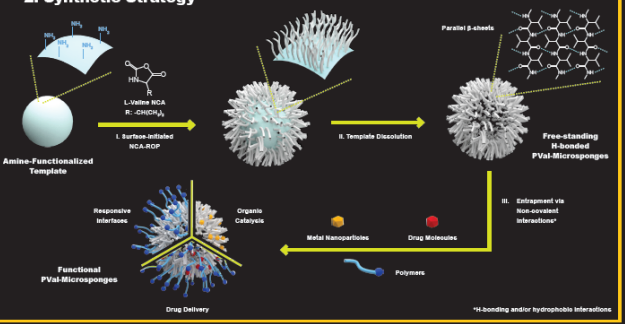

3. Results and Discussion

3.1. Synthesis of PVal-microsponges

Kinetic Study

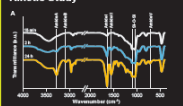

Figure 3.1.1. FT-IR spectra of PVal-coated silica particles after various SI-ROP time indicating β-sheets secondary structure. B) Increase of Amide I/ Si-O ratio with polymerization time indicating longer PVal grafts.

Morphology of Hollow PVal-microsponges

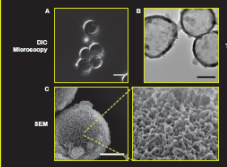

Figure 3.1.2. A) Differential interference contrast microscopy and B) TEM images of hollow PVal-microsponges isolated after 2 h of SI-ROP and subsequent template dissolution. C) SEM images reveal sponge-like morphology. Scale bars 5 μm for DIC image and 2 μm for TEM and SEM.

Size of PVal-microsponges

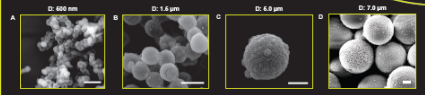

Figure 3.1.3. SEM images various PVal-microsponges fabricated by using non-porous silica template with diameter of A) 520 nm, B) 1.5 μm and C) 5 μm showing consistent sponge-like morphology. D) SEM images of PVal-coated mesoporous silica (D: 7 μm, pore size: 100 nm). Scale bars are 2 μm.

3.2. Entrapment of Metal

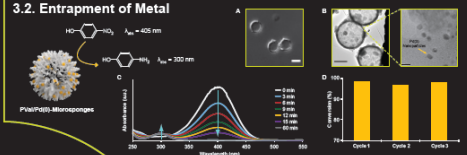

Figure 3.2. A) DIC microscopy and B) TEM images of Pd(0)-impregnated PVal-microsponges (scale bars are 5 μm, 2 μm and 10 nm) . C) Evolution of absorbance spectra with increasing hydrogenation reaction time. D) Conversion achieved in 60 min after 3 catalytic cycles.

3.3. Entrapment of Macromolecules

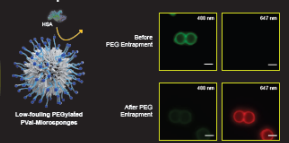

Figure 3.3. Fluorescent microscopy images showing reduction in human serum albumin (HSA; fluoresces green) fouling after the entrapment of polyethylene glycol) (PEG; fluoresces red).

3.4. Multiple macromolecules?

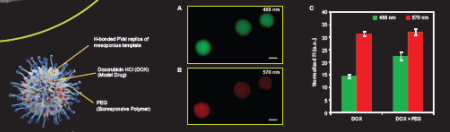

Figure 3.4. PVal negative-replica matrices fluoresces A) green at 488 nm and B) red at 570 nm after the entrapment of doxorubicin hydrochloride and PEG. C) Increase in fluorescent intensity at 488 nm associated with the conjugation of PEG488.

4. Conclusion

The present study demonstrates the facile formation of polypeptide microsponges by employing surface-initiated N-carboxyanhydride ring-opening polymerization. We further demonstrates the ability of the β-sheets-stabilized microsponges in entrapping a range of organic and inorganic materials including metal nanoparticles, proteins, drug molecules and bio-relevant polymers via non-covalent interactions.

Further studies are currently directed at employing this surface-driven approach to fabricate other unique β-sheets-assembled nano/micro-architectures, as well as utilizing the reported hollow PVal-microsponges as platforms for organic catalysis and biomedical devices.

5. References

1. H. R. Kricheldorf, Angew. Chem. Int. Ed. 2006, 45, 5752-5784

2. S. H. Wibowo, A. Sulistio, E. H. H. Wong, A. Blencowe, G. G. Qiao, Chem. Comm. 2014, 50, 4971-4988.

3. S. L. Goh, A. P. Platt, K. E. Rutledge, I. Lee, J. Polym. Sci. A Polym. Chem. 2008, 46, 5381-5389.

6. Acknowledgement

The authors acknowledge the Australian Research Council under Future Fellowship (FT110100411, G.G.Q.) scheme for financial support of this work. We also thank Dr. Matthew Rowles and Ka Noi for the assistance with XRD and HF treatment, respectively.

KINDSBEWEGUNGEN
DAS WISSEN DER FRAUEN

Heb. Josy Kühberger, Master-Thesis, APH-M 2011, FH Salzburg

HINTERGRUND

DIE MÜTTERLICHE WAHRNEHMUNG – eine Forschungslücke

Die sinnlichen Empfindungen der Frauen haben keinen Stellenwert in der herkömmlichen Schwangerenbetreuung. Deutungshoheit über alle körperlichen Vorgänge haben technische Hilfsmittel wie CTG, Ultraschall und Doppler. Wenn überhaupt, so wird das Auftreten regelmäßiger Kindsbewegungen als Hinweis auf fetales Wohlergehen ertragt.

Schwangere Frauen können jedoch neben der Häufigkeit auch die Art kindlicher Regungen detailliert beschreiben.

LEITFRAGE

WAS ERSPÜREN FRAUEN?

„Welche Wahrnehmungen beschreiben schwangere Frauen bezüglich des kindlichen Bewegungsverhaltens im letzten Trimenon?" – ein Beitrag zur praktischen Hebammenarbeit.

MATERIAL UND METHODEN

INTERVIEWS

- problemzentriert, leitfadengestützt
- vier Frauen mit unauffälligem Schwangerschaftsverlauf, Gestationsalter 38+5 bis 39+0, Einlingsschwangerschaft
- Frühling/Sommer 2013, Burgenland/Österreich
- Auswertung der transkribierten Audio-Aufnahmen durch zusammenfassende Inhaltsanalyse nach Mayring

ERGEBNISSE

DREI BEREICHE DER WAHRNEHMUNG

SENSORIELLE WAHRNEHMUNGEN

- Art der Bewegung (z.B. strecken, drehen, schieben…)
- Lokalisation der Bewegung
- bewegter Körperteil (Füße, Hände, Kopf, Rumpf)
- Intensität der Bewegung
- Schluckauf
- Ausformung neuer Bewegungsmuster

ZIRKADIAN-RHYTHMISCHE WAHRNEHMUNGEN

- Entwicklung eines tageszeit-abhängigen Auftretens der Bewegungen (Gemeinsamkeit: deutliche Aktivitätsspitze am Abend)
- Vertiefung verschiedener Verhaltenszustände (Schlaf, aktiver Wachzustand, ruhiger Wachzustand…)

REAKTIV-INTERAKTIVE WAHRNEHMUNGEN

- fortwährende Kommunikation zwischen Mutter und Kind
- wechselseitige Beeinflussung von mütterlicher und kindlicher Aktivität auf körperlicher und emotionaler Ebene
- zunehmende Reaktionsstthigkeit

ZUSAMMENFASSUNG

KINDSBEWEGUNGEN SIND GESUNDHEITSZEICHEN

Eine normale Entwicklung, besonders die des Gehirns, ist untrennbar mit der Austormung entsprechender Bewegungsmuster verwoben (Einspieler et al. 2012). Die Frauen zeichnen in ihren Wahrnehmungen also die Ausreifung neuromotorischer Kompetenzen ihrer Ungeborenen nach.

Typische Veränderungen im Bewegungsmuster können als **Hinweis auf physiologische Reifungs- und Vorbereitungsprozesse in Richtung Geburt** beobachtet werden.

Zum Beispiel

- Schluckauf als Vorbereitung auf die eigenständige Atmung (Kahrilas & Shi 1997; Piontelli 2006).
- abendliches Aktivitäts-Hoch als Ausdruck der zunehmenden Reife des zirkadianen Systems (Rivkees 2003)
- das Einsetzen von Schub- und Drehbewegungen des Kopfes als Instrument zur zeitlichen Einschätzung des Geburtsbeginns
- die Abnahme von Drehbewegungen des Körpers („Stellungswechsel") in den letzten Wochen als prognostisch günstiger Hinweis auf ein Tiefertreten des Kopfes, beginnende hormonelle Umstellung, eine gute Adaption im Beckeneingang und das Näherrücken der Geburt
- Vertestigung einzelner Verhaltenszustände (Non-REM-Schlaf, REM-Schlaf, ruhiger Wachzustand und aktiver Wachzustand) als Reife- und Gesundheitszeichen (de Vries & Fong 2006)

Das Ertragen der Kindsbewegungen gibt darüber hinaus Einblick in die Tiefe der bestehenden Bindung zwischen Frau und Kind. Denn die Fähigkeit kindliche Signale zu empfangen und die Bedürfnisse der Ungeborenen zu verstehen gilt als Hauptindikator einer vorgeburtlichen Mutter-Kind-Bindung (Shin et al. 2006).

SCHLUSSFOLGERUNG

DIE ERSPÜRNISSE NUTZEN

Die Wahrnehmungen der Frauen können in der praktischen Hebammenarbeit **als Instrument zur Beurteilung kindlichen Wohlbefindens** und der Reifungs- und Vorbereitungsprozesse Richtung Geburt dienen.

Fachhochschule Salzburg University of Applied Sciences

Kontakt
kuehberger.j@aon.at
Die vollständige Arbeit kann bei der Autorin angefragt werden.

Literatur
de Vries, JI.; Fong, BF.: Normal fetal motility: an overview. Ultrasound Obstet Gynecol 27:701-11 (2006)
Einspieler, C.; Prayer, D.; Prechtl, H.: Fetal Behaviour: A Neurodevelopmental Approach. Mac Keith Press, London (2012)
Kahrilas, PJ.; Shi, G.: Why do we hiccup? Gut 41:712-713 (1997)
Piontelli, A.: On the onset of human fetal behavior. In: Manca, M. edit.: Psychoanalysis and Neuroscience. 391-418. Springer Verlag, Mailand (2006)
Rivkees, SA.: Developing circadian rhythmicity in infants. Pediatrics 112(2):373-381 (2003)
Shin, H.; Park, YJ.; Kim, MJ.: Predictors of maternal sensitivity during the early postpartum period. J Adv Nurs 55(4):425-434 (2006)

Do missing megafauna limit the distributions of some trees?

Benjamin J. Seliger and Jacquelyn L. Gill
Climate Change Institute and School of Biology and Ecology, University of Maine, Orono, ME

The Problem

The mysterious fruits of some trees are best explained when viewed in the megafauna filled world in which they evolved[1] (Fig. 1). Tree species like Joshua Tree, which produce fruit largely uneaten today, were among common foods of now-extinct megaherbivores[2,3]. Since the Pleistocene megafaunal collapse, trees dependent upon these dispersers should have a reduced ability to track changing climates.

Figure 2: Pleistocene megaherbivores of the American Southwest that could potentially disperse large fruits included ground sloths, proboscideans, Pliestocene camels, and glyptodonts. Illustrations from Encyclopedia Brittantica.

Figure 1: Six North American fruit with adaptations for megafauna dispersal. Megafaunal fruit are often too large to eat or too difficult to open for extant animals, and are sugary or otherwise rich in nutrients. Many are not dispersed today.

We can test this hypothesis using the percentage a species realizes of its bioclimatically potential range as a proxy for dispersal during the Holocene[4]. On this poster, we estimate potential ranges with MaxEnt for Joshua Tree and Honey Mesquite, two species thought to have been dispersed by the community of megaherbivores that lived in the arid American Southwest[5] (Fig. 2). Results are shown as maps below.

The Data

Joshua Tree (*Yucca brevifolia*)

Holocene Dispersers: Secondary dispersal by seed-caching rodents[6]

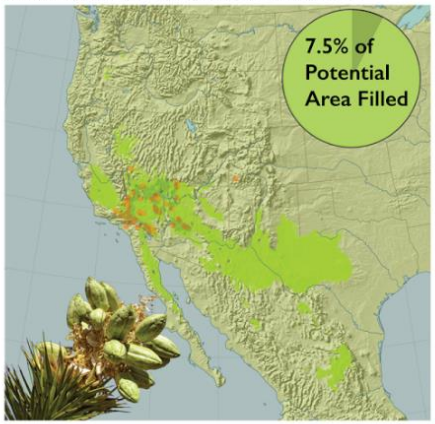

Honey Mesquite (*Prosopis glandulosa*)

Holocene Dispersers: Deer, coyotes, raccoons, skunks, turkeys and other birds[7]

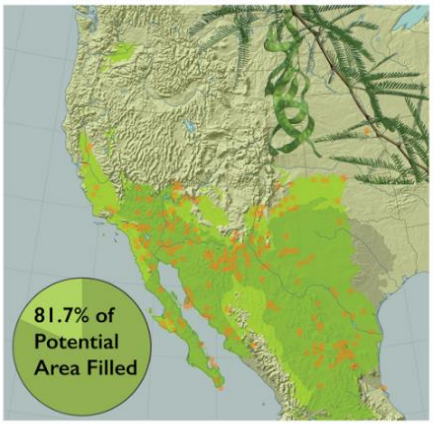

Legend
Occurrence
Potential Range
Realized Range

Joshua Tree and Honey Mesquite differ in the percentage of potential range filled by an order of magnitude. We attributed this difference to the disparity in Holocene dispersers between the two trees. Seed-caching rodents are the only documented dispersers of Joshua Tree today[6], while several mesofauna species disperse Honey Mesquite[7]. These preliminary data suggest that Joshua Tree's range could be limited due to the loss of megaherbivore dispersers. Future work is going to apply this analysis to suspected megafauna-dispersed species in Eastern North America.

Model Specifications
Method: MaxEnt
Occurrence data: GBIF
Climate Data: WorldClim & CGIAR
Evaluation: 80% training, 20% testing
Threshold: Sum specificity & sensitivity

Model Parameters
Environmental: GDD, avg. winter minimum, water balance, and precipitation seasonality
Realized: Range defined by USGS (E.L. Little)
Potential: Area predicted in atleast 4 out of 5 iterations each with different testing data

Contact info
benjamin.seliger@maine.edu

Literature Cited: 1. Janzen, D. H., & Martin, P. S. 1982. Science. 2. Harrington, M. R. 1933. Southwest museum papers. 3. Laudermilk, J. D., & Munz, P. A. 1934. Carnegie Institution of WA. 4. Svenning, J. C., & Skov, F. 2004. Ecology Letters. 5. Janzen, D. H. 1986. Annual Review of Ecology and Systematics. 6. Vander Wall, S. B., et al. 2006. Ecoscience. 7. Kneuper, C. L., et al. 2003. Journal of Range Management.

Molecular Dynamics Simulations of Periplasmic Proteins and Peptidoglycan in *Escherichia coli*

Pranav Laigudi

Gabriel Velez, Wesley Lay, Nick Fleege, Chengxuan Guo, Shuxiang Li, Casey Andrews, Dr. Adrian A. Elcock, Ph.D.

The Periplasm

1. Inner Membrane
2. Periplasm
3. Peptidoglycan
4. Outer Membrane

Figure 1: Anbaugram showing the layers of the *E. coli* cell wall

The periplasmic space of *E. coli* is an aqueous space between the two selectively permeable membranes around it. It contains a variety of soluble proteins as well as other solutes and ions. In *E. coli*, it contains a network of peptidoglycan, a mesh of sugars and amino acids, which is thinner in *E. coli*, a Gram negative bacterium, than Gram positive bacteria. It takes the pH of the extracellular environment, usually 7.5 or 7.0[1]. The periplasmic space is an important structure that plays a crucial role in protein export, and it can make up a substantial cellular portion, up to 40% of the volume of the cell[2].

Molecular Dynamics Simulations

Molecular Dynamics (MD) simulations are a powerful tool that can be used to visualize biological molecules and systems. They take coordinates for the atoms in a particular molecule and generate forces acting on them, based on physical and chemical principles and Newtonian dynamics, that act on other atoms within a certain cutoff radius[3]. Below is an example of a commonly used force field:

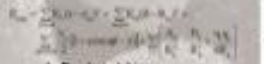

1. Bond stretching
2. Angle bending
3. Dihedral torsions
4. Electrostatic
5. Van der Waals

Figure 2: An MD simulation screenshot of the peptidoglycan layer

Simulation Information

The simulation was run on a PC computer cluster comprising 21 nodes, with 976 total cores, which possesses the ability to perform massive computations rapidly. The system of the 6 interlinked strands of peptidoglycan was simulated with the top 13 most abundant periplasmic proteins, randomly placed. It was solvated in water, and Na^+ and Cl^- ions were added at a concentration of 150 mM to balance the charge of the system. The AMBER99SBNMR1-ILDN force field was used, and the TIP4P-Ew water model was used. The production simulation was performed at 25 C.

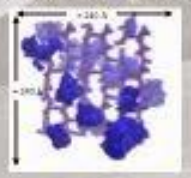

Figure 3: A screenshot of the set up configuration of the molecules. The proteins used in this simulation: Nucleoside Diphosphate Kinase, Thiol Peroxidase, Maltose Transporter, Ribonuclease, D-Ribose Transporter, Arginine Decarboxylase, TolB, Glucan Biosynthesis Protein, Glutamine Transporter, Galactoside Transporter. Protein is shown in blue, and carbohydrates are shown in red.

Methods

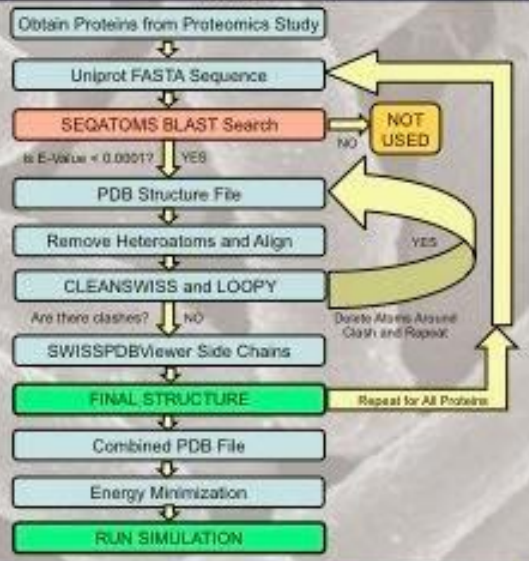

Protein Specifics

Structures generated for proteins in the periplasm are shown below with their structures and copy numbers, although only the first 13 are incorporated in the final simulation. Original template regions are shown in blue, while regions added by the modelling program are in red.

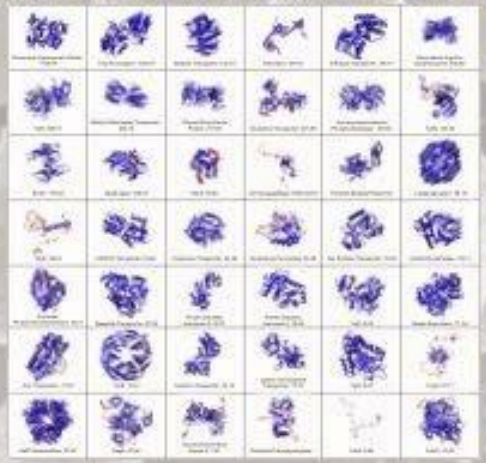

Simulation Results

Exploratory 5 ps simulations determined that 6 nodes and 288 cores (96 PME) should be used for optimal performance, yielding respectable __ ns/day in practice.

Conclusion

In this work, complete model structures for a large number of abundant periplasmic proteins were constructed. A ___ ns long molecular dynamics simulation of the 13 most abundant periplasmic proteins solvated within a box of water and ions, dispersed on either side of a 6 stranded model of the peptidoglycan was run. The interactions between the peptidoglycan layer and the proteins were examined, and ___

Implications

This simulation was another stepping stone on the way to constructing a model of the entire cell. Such a model would prove to be immensely helpful in all areas of the biological sciences, and would advance and revolutionize research, allowing for testing of biological hypotheses in in silico systems as well as allowing for verification of in vitro results. Future directions and the next steps to perform in the near future are to run simulations with the entire periplasmic protein fraction, and add the inner and outer membranes and proteins, and eventually the cytoplasm, to build a complete, accurate, and comprehensive model of the cellular structure.

Acknowledgements

I am extremely grateful to Dr. Elcock for the invaluable mentorship that he has provided throughout the project, as well as presenting me the incredible opportunity to work in his lab, as well as the amazing members of the lab for their guidance. In addition, I would like to sincerely thank Dr. Degner for her helpful advice and resources throughout this project.

References

1. [illegible]
2. [illegible]
3. [illegible]

Is the sediment an inexhaustible nutrient supply for benthic microalgae?

Sokratis Papaspyrou [1,2,a], Emilio García-Robledo [1,b], Julio Bohorquez [1], Juan-Luis Jiménez-Arias [1], Daniel Calenti [1], Alfonso Corzo [1]

Email: sokratis.papaspyrou@uca.es

Premise

Benthic microalgae (microphytobenthos, **MPB**) production is generally considered ***not*** to be **nutrient limited** due to an inexhaustible supply of nutrients from the sediment.

Net production relates to water column SiO_4^{4-}

Water column nutrients

An 18-month study of intertidal muddy sediments from the Bay of Cadiz (SW Spain) showed that **MPB net production rates** measured with microelectrodes were **best** explained by the water column **silicate** supply pattern (**18% of variation**).

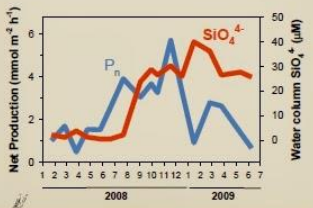

Sediment SiO_4^{4-} is limiting for MPB

Sediment nutrient pools

Analysis of the sediment nutrient pools (0-5mm layer) (i.e. porewater, freeze-lysable and KCl extractable) showed that **silicate** in these pools was **limiting** for MPB diatoms (Si/N<0.79).

In contrast, **no limitation** was found for either the water column or porewater **phosphorus** (N/P>21) .

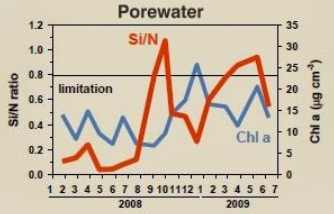

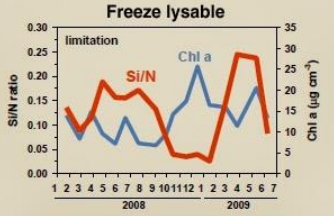

MPB production increases linearly with water column SiO_4^{4-} supply

Laboratory Si enrichment

Amendment of microcosms with silicate (0-35 µM) in laboratory experiments resulted in a linear increase of MPB normalised gross production.

Application of Monod-type semi-saturation curve estimated that ~100µM of silicate would be necessary to saturate MPB demand.

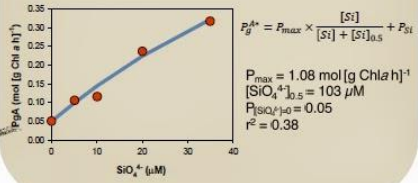

$$P_g^{A*} = P_{max} \times \frac{[Si]}{[Si] + [Si]_{0.5}} + P_{Si}$$

P_{max} = 1.08 mol [g Chl*a* h]$^{-1}$
$[SiO_4^{4-}]_{0.5}$ = 103 μM
$P_{[SiO_4^{4-}]=0}$ = 0.05
r^2 = 0.38

Conclusion

Silicate seems to be an central driving factor for MPB production in Cadiz Bay intertidal sediments

Sediment nutrients may be an important factor limiting MPB production during emersion periods.

1. Departmento de Biología, Universidad de Cádiz, Puerto Real, Spain
2. Instituto de Ciencias Marinas de Andalucía, CSIC, Puerto Real, Spain

Present addresses:
a. Departamento de Biotecnología, Universidad de Cádiz, Puerto Real, Spain
b. Section for Microbiology, Department of Bioscience, Aarhus University, Aarhus C, Denmark

Acknowledgements
AC: CTM 2009-10738 & CTM2013-43857-R (Ministry of Education and Science, Spain), P11-RNM-7199 (Andalusian Regional Government).
EGR: FPU grant (AP2005-4697) from Ministry of Education and Science
SP: JAE-Doc fellowship (Programa JAE, Spanish National Research Council) and a Marie Curie ERG action (NITRICOS, 235006, European Union).

Poster Resources

Better Posters: http://betterposters.blogspot.no/

Ten Simple Rules for a Good Poster Presentation: https://www.ncbi.nlm.nih.gov/pmc/articles/PMC1876493/

Designing conference posters: http://colinpurrington.com/tips/poster-design

Creating Effective Poster Presentations | An Effective Poster: https://projects.ncsu.edu/project/posters/